



Simulation and sensitivity analysis for cloud and precipitation measurements via spaceborne millimeter wave radar

Leilei Kou¹, Zhengjian Lin², Haiyang Gao¹, Shujun Liao², Piman Ding³

¹ Collaborative Innovation Center on Forecast and Evaluation of Meteorological Disasters, Key Laboratory for Aerosol-Cloud-Precipitation of China Meteorological Administration, Nanjing University of Information Science and Technology, Nanjing 210044, China

² School of Atmospheric Physics, Nanjing University of Information Science and Technology, Nanjing 210044, China

³ Shanghai Institute of Satellite Engineering, Shanghai 201109, China

Correspondence to: Leilei Kou (cassie320@163.com)

Abstract. This study presents a simulation framework for cloud and precipitation measurements via spaceborne millimeter wave radar composed of nine sub modules. To demonstrate the influence of the assumed physical parameters and optimizing the microphysical modeling of the hydrometeors, we first conducted a sensitivity analysis. The results indicated that the radar reflectivity was highly sensitive to the particle size distribution (PSD) parameter of the median volume diameter and particle density parameter, which can cause reflectivity variations of several to more than 10 dB. The variation in the prefactor of the mass-power relations that related to riming degree may result in an uncertainty of approximately 30–45 %. The particle shape and orientation also had a significant impact on the radar reflectivity. The spherical assumption may result in an average overestimation of the reflectivity by approximately 4–8 %, dependent on the particle shape and orientation modeling. Typical weather cases were simulated using optimal physical modeling accounting for the particle shapes, typical PSD parameters corresponding to the cloud precipitation types, mass-power relations for snow and graupel, and melting modeling. We present and validate the simulation results for a cold front stratiform cloud and a deep convective process with observations from W-band cloud profiling radar (CPR) on the CloudSat satellite. The simulated brightness band features, echo structure, and intensity showed good agreement with the CloudSat observations; the average relative error in the vertical profile was within 20 %. Our results quantify the uncertainty in the millimeter wave radar echo simulation that may be caused by the physical model parameters and provide a scientific basis for optimal forward modeling. They also provide suggestions for prior physical parameter constraints for the retrieval of the microphysical properties of clouds and precipitation.

1 Introduction

The development of clouds and precipitation is the result of interactions among dynamic, thermodynamic, and microphysical processes. The vertical structure of clouds is closely related to the characteristics of cloud radiation, as well as the physical process, mechanism, and efficiency of precipitation. Measurements of the three-dimensional (3D) structure and global distribution of cloud precipitation, as well as an understanding of the microphysical characteristics and transformation of

cloud precipitation, are the key factors affecting the accuracy of weather forecasting and climate models (Kollias et al., 2007; Li et al., 2013; Luo et al., 2008; Stephens et al., 2002).

35 According to the observation platform, cloud remote sensing can be divided into spaceborne, airborne, and ground-based measurements. Among them, spaceborne radar plays an important role in global cloud precipitation measurements owing to its strong penetration, high precision, and wide coverage. The most typical spaceborne radar is the millimeter wave cloud profiling radar (CPR) carried onboard the CloudSat satellite (Stephens et al., 2008; Tanelli et al., 2008). Since its launch, CloudSat CPR has obtained a large number of cloud vertical profile data, and has been widely used in cloud physics, weather, climate, environment and other fields (Dodson et al., 2018; Stephens et al., 2018; Battaglia et al., 2020).
40 Spaceborne millimeter wave radar can not only detect the vertical structure of various cloud systems, but also measure the distribution of snow, light rain, and even moderate rain (Haynes et al., 2009). It provides a comprehensive view of the water cycle by fully detecting clouds and associated precipitation (Behrangi et al., 2013; Ellis et al., 2009; Hayden et al., 2018).

Recently, many countries have begun research on next generation spaceborne cloud radar, thus demonstrating its detection capability (Battaglia et al., 2020; Illingworth et al., 2015; Tanelli et al., 2018; Wu et al., 2018), such as the CPR on
45 the EarthCARE satellite and dual-frequency cloud radar on the Aerosol/Clouds/Ecosystem (ACE) mission (Illingworth et al., 2015; Tanelli et al., 2018). In the design of the observation system and interpretation of cloud and precipitation observation data, forward modeling and simulation play a highly important role. QuickBeam is a user-friendly radar simulation package that compares modeled clouds to observations from CloudSat, but it cannot simulate mixed phase particles in the melting state. The Satellite Data Simulator Unit (SDSU) developed by Nagoya University, Japan, is a satellite multisensor simulator
50 integrating radar, microwave radiometer, and visible/infrared imager. Goddard Satellite Data Simulator Unite (G-SDSU) is a derivative version of the SDSU. In addition to the basic functions of the SDSU, it can be coupled with high-precision National Aeronautics and Space Administration (NASA) atmospheric models, such as the Weather Research and Forecasting-Spectral Bin Microphysics (WRF-SBM). The GPM satellite simulation is also based on the G-SDSU, which
55 converts the geophysical parameters simulated by the WRF-SBM into observable microwave brightness and equivalent reflectivity factor signals of the GPM. In traditional cloud data simulator or numerical models, the equivalent spherical shape is often used to calculate the scattering characteristics of the hydrometeor particles. However, the particle shape, composition, and orientation seriously affect the scattering characteristics. The density of mixed particles has a significant impact on the PSD parameters, which all cause uncertainties in cloud precipitation simulations.

China has also begun its own spaceborne millimeter wave radar project. The National Satellite Meteorological Center
60 plans to launch a cloud-detecting satellite, whose main load will be the cloud profiling radar. For development of spaceborne cloud radar, simulation research on cloud and precipitation detection can provide important theoretical support for the design and performance analysis of the system. In this study, we establish a simulation framework for spaceborne millimeter wave (94 GHz, W-band) radar detecting cloud and precipitation. Sensitivity analyses of typical cloud parameters, such as the particle size distribution (PSD) parameters, PSD model, particle density parameters, shape, and orientation, on the radar
65 equivalent reflectivity factors were carried out. Using optimization physical parameter settings, we present and compare the



simulation results of two typical cloud precipitation scenarios with measured CloudSat results. Based on a sensitivity analysis of typical cloud parameters and a demonstration of cloud precipitation cases, we show the radar reflectivity uncertainty caused by the physical modeling of hydrometeors while emphasizing the importance and necessity of assuming more realistic scattering characteristics, as well as appropriate density relation and PSD parameters corresponding to different cloud precipitation types.

2 Modeling

2.1 Overview

The forward modeling was mainly composed of nine sub modules: cloud precipitation scene simulation with Weather Research and Forecasting (WRF). WRF output result verification, hydrometeor microphysical characteristics modeling, particle scattering and attenuation characteristics calculations, atmospheric radiation transmission calculation, coupling with platform and instrument parameters, radar echo output, sensitivity analysis, and result comparisons and analyses. Figure 1 shows the logic structure between each sub module. First, we obtained the typical cloud precipitation scene cases from CloudSat historical data. According to the occurrence area and time, the corresponding National Center of Environmental Prediction Final (NCEP FNL) reanalysis data were obtained as the initial field in the WRF model. The WRF simulation result was verified by the observation data. Based on the hydrometeor mixing ratio of the WRF output, assuming certain microphysical parameters based on empirical information obtained from a large amount of observation data, the PSD of the hydrometeor particles were modeled. The complex reflective index of different hydrometeors was calculated according to the particle phase and temperature; the scattering and attenuation characteristics of the hydrometeor particles were then calculated using the T-matrix method. Meanwhile, the absorption coefficients of the atmospheric molecules, such as the water vapor and oxygen, were calculated based on the Liebe attenuation model. The radar reflectivity factor was then calculated, and the radar echo signal was obtained using the radar equation coupled with the instrument and platform parameters. During the simulation process, the sensitivity analysis of typical cloud physical parameters was performed so as to guide the optimization microphysical modeling of the hydrometeors. Finally, the simulation results were compared with observation data, such as CloudSat data, to validate the simulations.

2.2 Hydrometeor microphysical modeling

The radar reflectivity factor depends on the size, shape, orientation, density, size distributions, and dielectric constants for the hydrometeor particles. The microphysical characteristic of each hydrometeor was substantially different, which affects the scattering properties and then the radar echo. The following introduces the microphysical modeling of the different hydrometeors.



95 The complex refractive index of each hydrometeor was first calculated, which depends on their phase, composition, density, and radar wavelength. For pure water and pure ice, such as raindrops, cloud water, and cloud ice, we calculated the refractive index according to Ray (1972). Dry snow is a mixture of air and ice, while wet snow and graupel are a mixture of air, ice, and water. The densities of air, ice, and water are generally 0.001, 0.917, and 1 g/cm³, respectively. The mixture has different densities according to the proportions of different components. Given the proportion of air, ice, and water (or
100 riming fraction or melting fraction) in the hydrometeor, the refractive index of the mixture can be calculated using the Maxwell-Garnet mixing formula.

2.2.1 Cloud water

Cloud water droplets form from the condensation of super-saturated water vapor onto cloud condensation nuclei. They are usually spherical due to surface tension, with a typical size of ~10 μm. As the size of cloud droplets is small relative to the
105 wavelength, with an approximately spherical shape, their scattering characteristics can usually be calculated via Mie theory or Rayleigh approximation based on the sphere assumption. The PSD of cloud water can generally be modeled with a normalized Gamma distribution:

$$N(D)dD = N_w \frac{6}{3.67^4} \frac{(3.67 + \mu)^{\mu+4}}{\Gamma(\mu+4)} \left(\frac{D}{D_0}\right)^\mu \exp\left[-(3.67 + \mu)\frac{D}{D_0}\right] dD, \quad (1)$$

$$N_w = \frac{W}{\pi \rho_w} \left(\frac{3.67}{D_0}\right)^4, \quad (2)$$

110 where N_w is the normalized intercept parameter, D_0 is the median volume diameter, ρ_w is the density of water, i.e. 1 g/cm³, μ is the shape parameter, and Γ is the gamma function. Here, W in Eq. (2) is the water content of the cloud water, which is calculated by converting the mixing ratio of the hydrometeor from the WRF output:

$$W = \frac{P}{R_{gas} T} * 1000 * q, \quad (3)$$

where R_{gas} is the gas state constant, P is the air pressure in hPa, T is the temperature in K, q is the mixing ratio of the
115 hydrometeor based on the WRF output in kg/kg, and the units of W are g/m³. As W is the output of the WRF model, the PSD of the gamma distribution was mainly determined by two parameters, i.e., D_0 and μ . According to Miles et al. (2000) and Yin et al. (2011), we simulated the PSD with a D_0 and μ ranging from 0.005–0.05 mm and 0–4, respectively.

2.2.2 Rain

Owing to the effects of surface tension, aerodynamic force, and hydrostatic gradient force, raindrops often take the shape of
120 an oblate spheroid (horizontal axis (a_0) > vertical axis (b_0)), with an increase in the size of the raindrop. Here, we used the axis ratio model proposed by Brandes (2002):



$$\gamma_w = \frac{b_0}{a_0} = 0.9951 + 0.0251D - 0.03644D^2 + 0.005303D^3 - 0.0002492D^4, \quad (4)$$

where D is the equivolume diameter. The scattering and attenuation characteristics of raindrops were calculated using the T-matrix method. Considering the influence of aerodynamics on the direction of raindrop particles, the canting angle of raindrops was assumed to be a Gaussian distribution with a mean value of 0 and a standard deviation (SD) of 7° (Zhang, 2017).

The PSD of raindrops was still modeled as the Gamma distribution shown in Eqs. (1) and (2), where W was calculated based on the rain mixing ratio from the WRF output. According to Bringi (2001), D_0 and μ were uniformly distributed in ranges of 0.5–2.5 mm and –1 to 4, respectively.

2.2.3 Cloud ice

Cloud ice is mainly composed of various non-spherical ice crystals; the size and shape of ice crystal particles are complex and diverse, which depend on the cloud temperature and whether the particles have experienced collision and merging processes in the cloud (Heysfield et al., 2013; Ryzhkov and Zrníc, 2019). The database in Liu (2008) can be used to examine the scattering characteristics of ice crystals with different shapes. Here, we used the T-matrix to calculate the scattering properties of ice crystals: spheroid and cylinder were mainly considered as the shapes. The spheroid was treated as a horizontally aligned oblate spheroid with an axial ratio of 0.6 (Hogan et al., 2012); the relation between the larger and smaller dimension of cylinder was as follows (Fu, 1996):

$$\begin{cases} D/h = 5.068D^{0.586} & D > 0.2 \text{ mm} \\ D/h = 2 & D \leq 0.2 \text{ mm} \end{cases}, \quad (5)$$

The distribution of the orientations in ice particles is variable, which depends on their falling behavior. According to Melnikov and Straka (2013), we set the ice crystal orientations as a Gaussian distribution, with a mean canting angle of 0° and SD between 2° and 20° .

The PSD of cloud ice is similar to that of raindrops, mainly as an exponential or Gamma distribution. Here, the normalized Gamma distribution was adopted; the relation between the number concentration, N_w , and D_0 is as follows:

$$N_w = \frac{W}{\pi\rho_i} \left(\frac{3.67}{D_0} \right)^4, \quad (6)$$

where ρ_i is 0.917 g/cm³ and W is the water content of cloud ice from WRF output.

According to Heymsfield et al. (2013), the total number concentration, N_t , is a function of the temperature, T :

$$N_t = \begin{cases} 2.7 \times 10^4 & T \leq -60^\circ\text{C} \\ 3.304 \times 10^3 \exp(-0.04607T) & T > -60^\circ\text{C} \end{cases}, \quad (7)$$

The maximum diameter, D_{max} , is also dependent on T :



$$D_{\max} = \begin{cases} 11 \exp(0.069T) & \text{stratiform} \\ 21 \exp(0.070T) & \text{convective} \end{cases}, \quad (8)$$

150 where T is in °C, N_t is in m^{-3} , and D_{\max} is in mm. Given T and the water content of cloud ice, W , as well as the empirical value of μ , we can solve D_0 from Eqs. (1), (6)– (8) and the following formula:

$$N_t = \int_0^{D_{\max}} N(D) dD, \quad (9)$$

Owing to the monotonicity of the functions, D_0 can be easily solved numerically. For cloud ice, μ usually ranges from 0 to 2 (Tinel et al., 2005; Yin et al., 2011).

155 2.2.4 Snow

Snowflakes are usually caused by the conglomeration and growth of ice crystals. Although the shapes of snowflakes are irregular, they can also be modeled as spheroids, typically with a constant axis ratio of 0.75 (Nowell et al., 2013; Zhang, 2017). As snowflakes fall with their major axis mainly aligned in the horizontal direction, the mean canting angle of snow is normally assumed to be 0° and the SD of the canting angle is assumed to be 20° (Zhang, 2017). The width of the canting angle distribution grows with an increase in aggregation. Garrett et al. (2015) showed that the average SD of moderate-to-heavy snow, consisting of dry aggregates, is approximately 40° .

The PSD of graupel is modeled as an exponential distribution; the distribution parameters are constrained by the mass-power function relationship (Kneifel et al., 2011; Lin et al., 2011; Matrosov et al. 2007; Tomita, 2008):

$$N(D)dD = N_0 \exp(-\Lambda D)dD, \quad (10)$$

$$165 \quad m(D) = aD^b, \text{ or } \rho_s(D) = \frac{6}{\pi} aD^{b-3}, \quad (11)$$

$$\Lambda = \left[\frac{aN_0\Gamma(b+1)}{W} \right]^{\frac{1}{b+1}}, \quad (12)$$

where N_0 is the intercept parameter (usually between 10^3 – $10^5 \text{ mm}^{-1} \text{ m}^{-3}$) and $m(D)$ and $\rho_s(D)$ are the mass and density of the particle, respectively.

170 Constants a and b strongly depend on the snow habit and microphysical process that determine snow growth, which are usually determined experimentally. The exponent value of b is generally a Gaussian distribution, with a mean of 2.1 (Heymsfield et al., 2010; Von et al., 2017). The prefactor of a can vary considerably, and the value of a increases with the aggregate density or riming degree (Huang et al., 2019; Ryzhkov and Zrnicek, 2019; Sy et al., 2020; Wood et al., 2015). Most of the mass and density relations in previous studies (Brandes et al., 2007; Sy et al., 2020; Szyrmer and Zawadzki, 2010; Tiira et al., 2016) showed that the prefactor a between 0.005 and 0.014 cgs units (i.e., in g/cm^b), where D and m are in centimeters and grams; the mean value is approximately 0.009. The relations in different studies (Brandes et al., 2007;



Mason et al., 2018; Tiira et al., 2016; Wood et al., 2015) vary slightly: the primary difference is the diameter expression for the maximum dimension diameter, D_m , median volume diameter, D_0 , or volume equivalent diameter, D . In this study, the diameter in the mass and density relations were converted to D according to the assumed axis ratio.

2.2.5 Graupel

180 Graupel is generated in convective clouds by the accretion of supercooled liquid droplets on ice particles or by the freezing of supercooled raindrops lofted in updrafts. Actual graupel altitudes are highly variable because graupel is often observed in deep convection systems with strong up- and downdrafts. The density of graupel varies substantially depending on their formation mechanism, time of growth from the initial embryo, liquid water content, and ambient temperature. It is generally between 0.2 and 0.9 g/cm³; the typical value is 0.4 g/cm³ (Heymsfield et al., 2018; Ryzhkov and Zrníc, 2019).

185 Generally, graupels have irregular shapes. Here the shape of graupel was modeled as a spheroid, where the axis ratio was modeled as (Ryzhkov et al., 2011):

$$\begin{aligned} \gamma_g &= 0.8 & f_w &\leq 0.2 \\ \gamma_g &= 0.88 - 0.4f_w & 0.2 < f_w < 0.8 \\ \gamma_g &= 2.8 - 4\gamma_w + 5(\gamma_w - 0.56)f_w & f_w &\geq 0.8 \end{aligned} \quad (13)$$

where γ_w is the axis ratio of raindrops, and f_w is the mass water fraction. The SD of the canting angle, δ , was parameterized as a function of f_w :

190
$$\delta = 60^\circ(1 - cf_w), \quad (14)$$

where c is an adjustment coefficient, set usually as 0.8 (Jung et al., 2008).

The PSD of graupel is still assumed to be an exponential distribution, as shown in Eqs. (10)–(12). In convective clouds, a large part of graupel likely develops via collisions between frozen drops and smaller droplets; its bulk density decreases with an increasing graupel size (Khain and Pinsky, 2018). Similar mass relations can be found for graupel, but exponent b is higher compared with snow. Exponents for low-density graupel are approximately 2.3 (Erfani and Mitchell, 2017; von Lerber et al., 2017) while lump graupel approaches 3.0 (Mace and Benson, 2017; Mason et al., 2019). The mean value of b is approximately 2.6 and prefactor a varies mainly between 0.002 and 0.006 g/cm^b (Mason et al., 2018; Heymsfield et al., 2018), where the units for m and D are in grams and centimeters.

2.2.6 Melting modeling

200 Neglecting evaporation and the small amount of water that may collect on the particle owing to vapor diffusion, during the evolution process of snow from dry snow to wet snow and complete melting into water, we assumed that the mass of snow was conserved:

$$\rho_w D_w^3 = \rho_{ms} D_{ms}^3 = \rho_s D_s^3, \quad (15)$$



where ρ_w is density of liquid water, D_w is the water diameter, D_{ms} and D_s are the diameters of the melting snow and dry snow, respectively, and ρ_m and ρ_s are the densities of the melting and dry particles, respectively.

If the mass fraction of melt water in the particle of f_w is known, the density of melting snow can be obtained as follows (Haynes et al., 2009):

$$\rho_{ms} = \frac{\rho_s \rho_w}{f_w \rho_s + (1 - f_w) \rho_w}, \quad (16)$$

Besides, the density of snowflakes follows the power-law relation in Eq. (11). The exponent b in Eq. (11) can be approximately set as 2.1 and coefficient a can be obtained according to the exponential relationship between the density and diameter, where density is calculated from Eq. (16) with an assumed f_w value.

Due to melting, the uniform bin size set no longer applies, such that a new bin size must be calculated. According to Eqs. (11) and (15), the relation between the particle diameters can be obtained as follows:

$$D_w = \left(\frac{6}{\pi} a \right)^{\frac{1}{3}} D_{ms}^{\frac{b}{3}}, \quad (17)$$

where the equivalent-mass melted diameter D_{ms} corresponding to diameter D_s of each dry snow particle was calculated from Eq. (15).

The bin size for rain (dD_w) can be obtained by differentiating as follows

$$dD_w = \frac{b}{3} \left(\frac{6}{\pi} a \right)^{\frac{1}{3}} D_{ms}^{\frac{b-3}{3}} \cdot dD_{ms}, \quad (18)$$

According to the mass conservation model, the total liquid water content of a distribution is conserved. The number concentration of raindrops (N_w) in each size was calculated as follows

$$N_w = N_{ms} (D_{ms}) \frac{3}{b} \left(\frac{6}{\pi} a \right)^{-\frac{1}{3}} D_{ms}^{\frac{3-b}{3}}, \quad (19)$$

where $N_{ms} (D_{ms})$ is the number concentration of melting particles.

2.3 Radar equation

The signal power, P_r , received by the radar was calculated based on the radar equation:

$$P_r = C \frac{P_t}{r_0^2} Z_e \exp \left[-2 \int_0^{r_0} k(r) dr \right], \quad (20)$$

where P_t is the transmitted power, r_0 is the range to the atmospheric target, C is the radar constant related to the instruments, and k is the attenuation coefficient. The radar equivalent reflectivity factor, Z_e , was calculated from the scattering characteristics and the assumed PSD of the various hydrometeors:



$$Z_e = \frac{\lambda^4}{\pi^5 |K_w|^2} \int_0^\infty N(D) \sigma_b(D) dD, \quad (21)$$

230 where $\sigma_b(D)$ is the backscattering cross section of the particle with a diameter D , λ is the radar wavelength, and $K_w = (n_w^2 - 1) / (n_w^2 + 2)$, where n_w is the complex refractive index of water for a given wavelength and temperature.

For spaceborne millimeter wave radar, the equivalent radar reflectivity factor (hereafter, radar reflectivity) observed by the radar is the attenuated radar reflectivity factor, Z_{e0} :

$$Z_{e0} = Z_e \exp\left[-2 \int_0^{r_0} k(r) dr\right], \quad k = 10^{-3} \int Q_t(D) N(D) dD, \quad (22)$$

235 where the units of k are 1/km, Q_t is the extinction section of the corresponding hydrometeor calculated by the T-matrix (mm^2), the units of $N(D)$ are $\text{m}^{-3} \text{mm}^{-1}$, and the unit of dD is mm. In the actual simulation process, a look-up table of backscattering and extinction cross-sections is established for reducing the calculation workload, which is under different diameters, temperatures, and liquid water volume ratios according to the physical models of the hydrometeors.

If there are many types of hydrometeors at the same height, the equivalent radar reflectivity of each hydrometeor is
240 calculated based on the look-up table; then, the total radar reflectivity at this height is obtained by adding all types of hydrometeors. Considering the difference between the resolution of the simulation data and the observation resolution of the instrument, the convolution of the simulation echo and antenna pattern were also performed during the coupling process of the simulation data and instrument parameters, in which the antenna pattern was set as a two-dimensional Gaussian distribution.

245 After coupling with the antenna pattern, the final radar reflectivity was obtained. Here, Z_e has units of mm^6/m^3 and it is usually expressed in decibel form as $dBZ_e = 10 * \log_{10}(Z_e)$.

3 Sensitivity analysis

Due to complex microphysical processes in cloud precipitation, the PSDs of hydrometeors vary substantially; an accurate PSD is difficult to measure, especially for aloft particles. Besides, the phase, size, and shape of particles also change with the
250 microphysical process and external environment, which all affect the simulation results. For optimizing the parameter settings of the forward modeling and more accurately interpreting the radar reflectivity results, we performed a series of sensitivity analyses of typical cloud parameters. Here, we mainly focused on the scattering effects; the attenuation effects will be discussed in a follow-up study.



3.1 PSD parameters

255 The Gamma distribution is determined by three parameters. As one of the parameters is obtained from the water content, W , of the hydrometeor in the WRF output, we mainly considered the effects of D_0 and μ on the radar reflectivity. Figure 2 shows the change in the radar reflectivity with variations in the gamma PSD parameters for cloud water and rain. Cloud water particles are relatively small in wavelength, which is in the linear growth stage in the Mie scattering region; the larger D_0 corresponds to more large-size particles, which leads to stronger echoes. With a five-fold increase in D_0 , e.g., increasing
260 from 10 to 50 μm , leads to an increase in the reflectivity of approximately 20 dB. For rain particles, the impact of D_0 is not as significant as that of cloud water: a five-fold change in D_0 can lead to a change in the reflectivity within 5 dB. Owing to the Mie scattering effect on raindrops, the contribution from relatively small raindrops may be more than that from larger raindrops considering the influence of the number concentration. In the gamma PSD, the effect of μ is relatively small; the change in the reflectivity caused by μ is within 1.5 dB when using a constant D_0 .

265 For cloud ice, D_0 is calculated from Eq. (9) given W and T ; μ is the only parameter that needs to be assumed. Figure 3a and b show the reflectivity change with W and μ , where Fig. 3a was obtained when T was -20°C and Fig. 3b was obtained when T was -60°C . As the PSD of cloud ice was constrained by the total number concentration, D_0 and μ are interrelated and D_0 increases with an increase in μ , W , and T . Based on Fig. 3a and b, we observed that when μ varies from 0 to 2, the maximum reflectivity change is approximately 4 dB at -20°C while that at -60°C is approximately 5 dB. The reflectivity
270 change was still affected by the D_0 variation. Based on Eq. (9), D_0 varied from 0.1–0.5 mm at -60°C and 0.2–0.8 mm at -20°C when W ranged from 0 to 0.5 g/m^3 . Figure 3c and d show the reflectivity change caused by D_0 and μ under a conventional gamma PSD without constraints on the total number concentration. In the conventional gamma PSD, the D_0 and μ vary independently; the reflectivity can change by 13 dB when D_0 varies from 0.2 to 0.8 mm. The results showed that the effect of PSD parameter variation on the reflectivity can be reduced by approximately 60 % owing to constraints on the
275 total number concentration for the PSD of cloud ice.

An exponential PSD with a power-law mass spectrum was used for snow and graupel. Figure 4 shows the effects of intercept parameter N_0 and the mass power-law parameters of prefactor a and exponent b . With the mean mass-size relationships for snow and graupel, changing the dBN_0 ($\text{dBN}_0 = \log_{10}(N_0)$) from 3 to 5 could cause a reflectivity increase of approximately 7–8 dB. With a constant N_0 and mean value of exponent b , the reflectivity change caused by variation in
280 prefactor a from 0.005 to 0.013 g/cm^b for snow and 0.02 to 0.06 g/cm^b for graupel can reach 8–9 dB. Using an average mass-power relation assumption, the variation in a may result in an uncertainty of approximately 45 % and 30 % for snow and graupel, respectively. For snow and graupel, exponent b is approximately 2.1 and 2.6, respectively. For analyzing the effect of the variation in b , a Gaussian distribution of b was modeled. According to the range in b , the standard deviation (SD) was assumed to be 0.5 and 0.3 for snow and graupel, respectively. The error bars in Fig. 4c and f represent the SD of the



285 reflectivity change caused by variation in b , which was generally less than 2 dB for snow and 0.5 dB for graupel. The results showed that the sensitivity of reflectivity to prefactor a was substantially greater than that of exponent b .

3.2 PSD models

The PSDs of hydrometeors can usually be represented as different models, such as the Gamma distribution and lognormal distribution, which are frequently used in cloud water PSDs. This section discusses the influence that the selection of
290 different PSD models has on radar reflectivity factor, taking cloud water as an example. Figure 5a shows two PSD models of cloud water, in which the black solid line represents the Gamma distribution, and the red-dotted line represents the lognormal distribution. The lognormal distribution uses the following formula:

$$N(D)dD = \frac{6W}{\pi\sqrt{2\pi}\rho_p\sigma D_m^3} \exp\left(-\frac{9}{2}\sigma^2\right) \exp\left[-\frac{(\ln D - \ln D_m)^2}{2\sigma^2}\right] \frac{dD}{D}, \quad (23)$$

where D_m is the mass weighted diameter, σ is the dispersion parameter.

295 The parameters in the PSD model in Fig. 5a are based on the typical parameter settings for cloud water in terrestrial stratiform clouds (Mason, 1971; Miles et al., 2000; Niu and He, 1995), where D_0 is 20 mm, μ is 2 in the Gamma distribution, D_m is 20 mm, σ is 0.5 in the lognormal distribution, and W in both PSD models are set to 1g/m^3 . The Gamma distribution (blue line) is the result of changing D_0 (black line) from 20 to 30 mm; the objective is to obtain similarity between the Gamma and log-normal models. Corresponding to the typical parameter settings of the Gamma and log-normal distributions,
300 the difference between the two PSDs was notable; the reflectivity caused by the different PSD models was approximately 4.5 dB. For the gamma distribution (D_0 of 30 mm and log-normal distribution), there was still a difference in the radar reflectivity of approximately 0.8 dB. This result showed that the PSD model had a certain impact on echo simulation; it was necessary to carefully select the PSD model and set the parameters according to the type of cloud and precipitation.

3.3 Particle shape and orientation

305 The scattering properties of particles are sensitive to the hydrometeor shape and orientation. Previous studies (Marra et al., 2013; Masunaga et al., 2010; Seto et al., 2021; Wang et al., 2019) often assume that the hydrometeor particle is a sphere, but most particles are non-spherical. This section discusses the influence that cloud ice, snow, graupel, and rain particle shapes (cloud water is generally spherical) have on radar reflectivity.

Figure 6 compares the backscattering cross-section and corresponding radar reflectivity under different shapes of cloud
310 ice, dry snow, and rain. Three shape types, i.e., sphere, spheroid, and cylinder, for cloud ice were mainly considered, where the shape parameter setting refers to section 2.2.3. The solid and dotted lines in Fig. 6a indicate that the SD of the canting angle (δ) is 2° and 20° , respectively. The radar reflectivity factor in Fig. 6b was obtained with the constrained PSD parameter (section 2.2.3) of $T = -60^\circ\text{C}$ and $\mu = 1$. The backscattering difference for cloud ice was evident between the



sphere and non-sphere when the diameter was greater than 1 mm. Figure 6b shows that the spherical assumption may result
315 in an average overestimation of the reflectivity by approximately 6 %. The reflectivity difference caused by δ was
approximately 1 %. Figure 6c shows the backscattering section of dry snow with a constant density of 0.1 g/cm^3 , where the
axis ratio of the spheroid was 0.75 and the SD of the canting angle was assumed to be 20° and 40° , respectively. When
calculating the radar reflectivity factor, the corresponding exponential distribution parameter was $N_0 = 3 \times 10^3 \text{ m}^{-3} \text{ mm}^{-1}$ and
the average reflectivity difference between the sphere and spheroid reached approximately 8 % for a δ of 20° and 4 % for a
320 δ of 40° . For raindrops, the apparent backscattering difference appeared after the equivalent diameter was 2 mm, as shown
in Fig. 6e. The reflectivity in Fig. 6f was obtained with a Gamma PSD parameter of $D_0 = 1.25 \text{ mm}$ and $\mu = 3$. The reflectivity
difference caused by the particle shape was negligible. This is because particles less than 2 mm mostly contribute to the
radar reflectivity for rain. The influence of shape on raindrops can be negligible.

The axis ratio and particle orientation change with variations in the density of snow and graupel. Figure 7 compares
325 backscattering and corresponding radar reflectivity for graupel between spheres and spheroids at different densities and
orientations. The influence of particle shape on snow is similar to graupel (figures not shown here). The SD of the canting
angle in Fig. 7a was calculated according to Eq. (14). Here, δ was 54° at a density of 0.4 g/cm^3 while δ was 20° at a density
of 0.8 g/cm^3 . Based on Fig. 7a, the backscattering section difference increased with density, which may have been due to the
stronger refractive index. Figure 7b shows the corresponding radar reflectivity for particles in (a), where the PSD was
330 assumed to be an exponential distribution with N_0 of $4 \times 10^3 \text{ m}^{-3} \text{ mm}^{-1}$. The spherical assumption may cause an average
overestimation of the reflectivity by approximately 4 % when the density is 0.8 g/cm^3 and δ is 20° , whereas the reflectivity
difference is negligible at δ of 54° and density of 0.4 g/cm^3 . This result showed that, besides particle shape, the particle
density and orientation should also be considered in the scattering simulation.

4 Simulation results for typical cases

335 Based on the sensitivity analysis of typical cloud physical parameters, we simulated the radar reflectivity of typical cloud
scenes by assuming appropriate physical parameters for different hydrometeors and cloud precipitation types with the
hydrometeor mixture ratio from the WRF as input. The simulation results were compared with CloudSat observation data.
We then showed two typical weather cases: a cold front stratiform cloud and deep convective process.

4.1 Stratiform case

340 4.1.1 WRF scenario simulation

From September 24 to 25, 2012, there was a large-scale low trough cold front cloud system in northwest China, which
moved from the west to the east and entered Shanxi Province. The CloudSat satellite observed the stratiform cloud process



from 40.67°N, 118.22°E to 41.56°N, and 117.93°E at 04:23 AM on September 25, 2012. Centered on the observation range of CloudSat, this stratiform cloud process was simulated by the WRF model. This experiment adopted a one-way scheme with a quadruple nested grid. From the inside to the outside, the horizontal resolution was 1, 3, 9, and 27 km. It is divided into 40 layers vertically and the top of the model was 50 hPa.

Figure 8a shows the simulation area for the two internal layers (d03 and d04), in which the black line is the trajectory of the CloudSat CPR. Figure 8b shows the 3-D distribution of the total hydrometeor output of the WRF corresponding to the innermost grid. The hydrometeors were cloud water, snow, cloud ice, and rain. The hydrometeors were mainly distributed below 10 km; the maximum total water content was at approximately 3 km, $\sim 0.9 \text{ g/m}^3$.

Figure 8c–f compares the fraction of cloud cover and cloud top temperature simulated by the WRF with European Centre for Medium-Range weather Forecasts ReAnalysis 5 (ERA5) data and Moderate Resolution Imaging Spectrometer (MODIS) observation data. Considering the resolution of ERA5 data and the MODIS scanning track, the outermost grid in the WRF simulation data was used for comparison. Figure 8c and d show the fraction of cloud cover from the WRF model and ERA5 data, respectively. The WRF simulates the northeastern and southwestern zonal distribution of the cold front cloud system; the simulated cloud area and cloud coverage are consistent with the ERA5 data. Figure 8e and f compares the cloud top temperature from the WRF simulation and MODIS observations. Both exhibited low cloud top temperatures in the northeast and high cloud top temperatures in the south. The value, location, and distribution of cloud top temperatures simulated by the WRF were consistent with the satellite observations. The WRF accurately simulated the cloud system in this case, such that the cloud scenario simulation results are valid.

4.1.2 Radar reflectivity simulation results

For comparison with CloudSat data, the two-dimensional (2-D) hydrometeor profile from the WRF model on the track matching CloudSat was selected as the input for the radar reflectivity simulation. The WRF data at 04:30 AM was selected. Owing to the uneven output height layer of the WRF, data for the WRF simulation results were interpolated in the vertical direction; the vertical resolution of the interpolated data was 240 m, corresponding to the CloudSat CPR data.

Figure 9a–e shows the latitude-height cross-section of the hydrometeors in the stratiform case simulated by the WRF for cloud water, cloud ice, snow, rain, and the total hydrometeors. Snow is widely distributed, ranging from 3 to 10 km. Rain is widely distributed with water contents between 0.1 and 0.2 g/m^3 . At approximately 0 °C, the cloud water, snow, and rain were rich, which led to a high total water content, with a maximum of 0.57 g/m^3 .

For the stratiform case, the PSD parameters were assumed based on the typical empirical values of land stratiform precipitation clouds (Mason, 1971; Niu and He, 1995; Yin et al., 2011). As snow in stratiform clouds are mainly unrimed particles (Yin et al., 2017), a mass-power relation representative of unrimed snow (Moisseev et al., 2017) was used in the simulation. In addition, a melting layer model with a width of 1 km was assumed below 0 °C and the PSD parameters of the raindrops were calculated according to the melting model. Figure 9f–h shows the simulated radar reflectivity factor with the



375 total hydrometeors, where Fig. 9f shows the reflectivity before attenuation, Fig. 9g shows attenuation, and Fig. 9h shows
reflectivity after attenuation. The reflectivity factor above 8 km was mainly a result of weak cloud ice and dry snow, which
did not exceed -5 dBZ. The radar reflectivity caused by snow increased with an increase in the water content, up to
approximately 10 dBZ. Melting led to an increase in the refractive index and density of snow, which resulted in a sharp
increase in the radar reflectivity factor. Before attenuation, the radar reflectivity in the melting layer was equivalent to the
380 reflectivity in the rain region. After attenuation, the radar reflectivity showed a rapid signal decline at the end of the melting
region, and the bright band became evident.

For the 94 GHz radar, the Mie scattering effect was dominant; the scattering efficiency tended to be stable when the
particle reached a certain diameter. Although larger snowflakes melt and produce larger raindrops at depth in the melting
layer, their contribution to the reflectivity factor was not significant owing to a decrease in their number concentration.
385 Therefore, the bright band was not notable before attenuation; the reflectivity factor increased markedly in the upper part of
the melting layer but did not decrease considerably in the lower part. However, the bright band at the melting layer was
highlighted after attenuation owing to strong attenuation caused by rain, melting snow, and exponential growth of the
attenuation.

Figure 10 shows a radar reflectivity comparison between the simulation results and CloudSat CPR observation data. The
390 cross-sections in Fig. 10a and b show simulation results, where Fig. 10a corresponds to the optimization settings shown in
Fig. 9h, and Fig. 10b corresponds to the conventional setting that does not consider the mass-power relation of snow and the
melting model. Figure 10c shows the observation results from the CloudSat CPR. The lines in Fig. 10d show the average
vertical profiles of the reflectivity factor in Fig. 10a–c. The echo structure and echo intensity of the simulation results with
the optimization setting showed good agreement with the CloudSat observations. The trends in the two profiles were
395 basically identical; the relative error at each height was mostly within 15 %. The location and intensity of the brightness
band from the optimization simulation and CloudSat observation were highly consistent; the radar reflectivity peak for both
were approximately 12 dBZ at 2.88 km with a bright band width of approximately 0.9 km. Without the melting model, the
PSD parameters for raindrops were based on the assumed value. In Fig.10b, the radar reflectivity below 0 °C was evidently
stronger; the width and location of the strong echo band were considerably different from the bright band in the simulation
400 with the optimization setting and CloudSat observation. The relative error in the average profile below the melting layer
reached 40 %. The radar reflectivity peak in the vertical profile from the conventional simulation was 13 dBZ at
approximately 2.6 km with a bright band width of approximately 1.4 km. In summary, the melting model can accurately
capture the stratiform cloud precipitation characteristics; in other words, simulations with mass-power constrained PSD of
snow and the melting model are more similar to the observations.



405 4.2 Convective case

This case was a severe convective weather process that occurred in the Lower Yangtze-Huaihe river on June 23, 2016, in which strong winds and heavy rainfall occurred in Yancheng City, Jiangsu Province. The simulation area covered 32–36°N and 116–120.5°E. Triple nested grids were adopted, with horizontal resolutions of 13.5, 4.5, and 1.5 km. The model simulation results were compared with MODIS observation data and the cloud structure and cloud top temperature were
410 consistent (figure not shown).

CloudSat observed this convective process at 04:30 AM on June 23, 2016, covering the cloud region from 32.43°N, 119.13°E to 36.11°N, and 118.10°E. For comparison with the CloudSat data, the vertical cross-section of the hydrometeor matching the CloudSat observation was selected for simulation. Figure 11a–f shows the latitude-height cross-section of the hydrometeor for the convective case simulated by the WRF for the total hydrometeors, cloud water, cloud ice, snow, graupel,
415 and rain. The ice water content of the convective case was rich; the cloud ice, snow, and graupel particles were widely distributed with high contents. Snow existed from 4 to 14 km, with a water content reaching approximately 1.5 g/m³. Graupel particles mainly ranged from 4–8 km, with a maximum water content of 1.2 g/m³. Rain was mainly distributed between 34 and 36°N: the water content of the rain near 34.5 and 34.8°N reached 5 g/m³.

In the convective case, mixed phase particles, such as snow and graupel, were abundant while the components of snow
420 and graupel were complex. Unlike stratiform clouds, a large percentage of heavily aggregated and/or rimed snow exist in convective clouds (Yin et al., 2017); therefore, rimed particles were assumed for convective clouds modeling. As the prefactor a in the density-power relations increases with the riming degree (Mason et al., 2018; Moisseev et al., 2017; Ryzhkov and Zrnich, 2019), an adjustment factor f was considered in the simulation process, i.e., $a = a_u f$, where a_u is the density prefactor for unrimed snow, and f is obtained by $f = 1/(1 - FR)$ where FR is the ratio of the rime mass to the snowflake
425 mass. According to Mason et al (2018) and Moisseev et al (2017), we assumed that the rime mass fraction increased with linearly with liquid water path. The exponent b was assumed as the mean value (a constant) based on the sensitivity analysis. Then, the corresponding refractive index and PSD for snow and graupel were calculated according to the mass-power relations. The other physical parameters, such as the number concentration, were assumed according to the typical parameters of convective cloud precipitation (Ryu et al., 2021; Sun et al., 2020; Yang et al., 2019).

Figure 11g–i show the simulated radar reflectivity with the total hydrometeors, where Fig. 11g is the reflectivity before
430 attenuation, Fig. 11h is the attenuation, and Fig. 11i is the reflectivity after attenuation. Figure 11i shows that the internal vertical structure of the deep convective cloud can be accurately detected, but millimeter wave radar has difficulty penetrating the rainfall layer due to strong attenuation. Figure 12 shows a radar reflectivity comparison between the simulation results and CloudSat CPR observations for the deep convective case, where Fig. 12a–c shows the cross-sections of the reflectivity from simulations with optimization and conventional settings, as well as the CloudSat observations. The
435 main difference between the simulation processes in Fig. 12a and b is that the conventional setting used a constant density for snow and graupel while the density was varied according to the density-power relation of rimed particles in the



optimization setting. The lines in Fig. 12d are the average profiles corresponding to Fig. 12a–c. Figure 12a and c show that the echo distribution and echo intensity of the simulation and CloudSat observation are in good agreement. The echo top heights were approximately 16 km and the maximum reflectivity factor was approximately 18 dBZ. The hydrometeors for the cloud water, graupel, and rainfall particles were mainly concentrated between 34.5°N and 35.5°N, which produced strong echoes at middle heights and strong attenuation at lower heights. Comparing the profiles with the optimized simulation to that with the conventional simulation in Fig. 12d, the fixed density in the conventional simulation caused the echo at high altitudes to be stronger and the echo at low altitudes to be weaker.

To further illustrate the effect of snow and graupel, Fig. 13 shows the water content and reflectivity profiles for snow and graupel corresponding to the black line in Fig. 12a. Figure 13a shows the vertical profile of the water content of snow and graupel. Figure 13b shows the simulation results corresponding to the hydrometeor profile in Fig. 13a. Relative to the reflectivity results with the conventional simulation, snow and graupel in the optimization simulation showed weak echo at high altitudes and strong echo at low altitudes. The trend in the profile for snow and graupel in Fig. 13b is the same as that in the average profiles shown in Fig. 12d. The vertical profile in the optimization simulation showed good consistency with that of the CloudSat observation, with an average relative error of approximately 20 %. In contrast, the average relative error in the conventional simulation reached approximately 100 %. The simulation results demonstrated that the radar reflectivity is highly sensitive to the prefactor of the mass-power relation of snow and graupel; the effect of riming on the prefactor should be considered in the forward modeling simulations or microphysical parameter retrieval for convective clouds.

5 Conclusions

Active remote sensing with spaceborne millimeter wave radar is one of the most effective means of cloud and precipitation measurements. Many countries are developing next generation spaceborne cloud precipitation radar. During the design and demonstration stage of observation systems and in the interpretation of observation data, forward modeling simulations play a crucial role. The physical characteristics of hydrometeor particles, such as the shape, density, composition, PSD model and parameters, have an important impact on the simulation results. Based on establishing a simulation framework with nine sub modules, we quantified the uncertainty of different physical model parameters for hydrometeors via a sensitivity analysis, presenting radar reflectivity simulations with optimized parameter settings.

The sensitivity of D_0 in the Gamma distribution was approximately 5–10-fold greater than that of μ ; the variation in μ can cause reflectivity changes of less than 10 %. The constraints on PSD modeling from the empirical relationships in the observations using interconnected parameters, rather than independent variations, can significantly reduce the impact of PSD variation. Owing to the constraint on the total number concentration for the PSD of cloud ice, the effect of D_0 on the radar reflectivity can be reduced by approximately 60 %. The particle density not only affects the shape and orientation of particles, but also affects the size distribution of the particles. Using the exponential PSD with a power-law density spectrum for snow and graupel, we found that the effects of prefactor a were significantly greater than that of exponent b ; variation in a may



470 result in an uncertainty of approximately 45 % for snow and 30 % for graupel. Owing to complex physical characteristics
resulting from various microphysical processes, the shape and orientation of frozen and mixed phase particles are variable,
which could lead to an average reflectivity difference of approximately 4–8 %. In addition to the PSD parameter and particle
shape and orientation, this study emphasized the importance of the particle density parameters and PSD modeling constraints
corresponding to different cloud precipitation types in the forward simulation and microphysical properties retrieval.

475 Two typical cloud precipitation cases were presented. The simulation results were compared with the CloudSat
observations. During simulation, we considered the PSD parameter settings for typical cloud precipitation types, particle
shapes, melting model, and influence of snow and graupel density relations. For snow and graupel microphysical modeling,
unrimed snow particles was assumed in the stratiform clouds, and rimed snow with varying density-power relations was
considered in the convective clouds. The simulation results with the optimization setting showed good agreement with the
480 CloudSat observations; the average relative errors in the vertical profile between the simulation and CloudSat data were
within 20 %, which improved by 20–80 % compared with the conventional setting, i.e., not considering the melting model
and riming effect for snow and graupel. The melting layer modeling for stratiform cloud could accurately reproduce the
bright band structure after attenuation. The varying prefactor of density relations of snow and graupel considering the riming
effects for convective cloud rendered the simulated echo structure consistent with the observations.

485 The selection and modeling of cloud microphysical characteristics not only affects the forward simulation and
numerical modeling, but also has a significant impact on physical parameter retrieval. This study contributes to a quantitative
understanding of the uncertainties of forward simulations or radar retrievals due to variation in the microphysical properties
of hydrometeors. They also provide a scientific basis for the analysis of millimeter wave radar observation data, the
optimization of parameter settings in forward modeling, and microphysical constraints in parameter retrievals. The
490 sensitivity test and simulation results suggest that accurate estimation of at least two parameters in the size distributions of
hydrometeor particles including particle density factor is beneficial using certain methods, such as multiband measurements.
Sensitivity to the particle shape and orientation demonstrates that increasing the polarization function is useful for analyzing
the microphysical properties of frozen and mixed hydrometers. In future studies, we will consider establishing a cloud
database for further optimizing prior information constraints by collecting a large amount of typical cloud precipitation
495 microphysical observation data at different climatic regions.

Data availability. The NCEP FNL reanalysis data for driving WRF model simulation are available at
<https://rda.ucar.edu/datasets/ds083.2>. The CloudSat data are available at <https://www.cloudsat.cira.colostate.edu/data-products>.

500

Author contributions. LL and ZJ carried out the sensitivity analysis, weather case simulation experiment and data analysis;
HY and SJ carried out the WRF model simulation and provided the input. PM provided technique support and analysis
methods. LL wrote the original article with feedback from all the coauthors.



505 *Competing interests.* The authors declare that they have no conflict of interest.

Acknowledgements. We acknowledge the data providers of the National Centers for the Environmental Prediction Final Operational Model Global Tropospheric Analyses. We would like to thank the scientists and those who contribute to CloudSat mission. This study was supported in part by the National Key Research and Development Program of China
510 (2021YFC2802502), in part by the National Natural Science Foundation of China (41975027).

References

- Battaglia, A., Kollias, P., Dhillon, R., Roy, R., Tanelli, S., Lamer, K., Grecu, M., Lebsock, M., Watters, D., Mroz, K., Heymsfield, G., Li, L. H., and Furukawa, K.: Spaceborne cloud and precipitation radars status challenges and ways forward, *Rev. Geophys.*, 58, e2019RG000686, doi: 10.1029/2019RG000686, 2020.
- 515 Behrangi, A., Tian, Y. D., Lambriksen, B., and Stephens, G. L.: What does CloudSat reveal about global land precipitation detection by other spaceborne sensors? *Water Resour. Res.*, 50, 4893–4905, doi:10.1002/2013WR014566, 2013.
- Brandes, E., Ikeda, K., Zhang, G., Schoenhuber, M., & Rasmussen, R.: A statistical and physical description of hydrometeor distributions in Colorado snowstorms using a video disdrometer, *J. Appl. Meteorol. Climatol.*, 46, 634–650, doi: 10.1175/JAM2489.1, 2007.
- 520 Bringi, V. N., and Chandrasekar, V.: *Polarimetric Doppler weather radar: principles and applications*, New York, NY: Cambridge Univ., 2001.
- Dodson, J. B., Tylor, P. C., and Branson, M.: Microphysical variability of Amazonian deep convective cores observed by CloudSat and simulated by a multiscale modeling framework, *Atmos. Chem. Phys.*, 18, 6493–6510, doi: 10.5194/acp-18-6493-2018, 2018.
- 525 Ellis, T. D., L’Ecuyer, T., Haynes, J. M., and Stephens, G. L.: How often does it rain over the global oceans? The perspective from CloudSat, *Geophys. Res. Lett.*, 36, L03815, doi:10.1029/2008GL036728, 2009.
- Erfani, E., and Mitchell, D. L.: Growth of ice particle mass and projected area during riming, *Atmos. Chem. Phys.*, 17, 1241–1257, doi: 10.5194/acp-17-1241-2017, 2017.
- Fontaine, E., Schwarzenboeck, A., Leroy, D., Delanoë, J., Protat, A., Dezitter, F., Strapp, J. W., and Lilie, L. E.: Statistical
530 analysis of ice microphysical properties in tropical mesoscale convective systems derived from cloud radar and in situ microphysical observations, *Atmos. Chem. Phys.*, 20, 3503–3553, doi: 10.5194/acp-20-3503-2020, 2020.
- Garrett, T., Yuter, S., Fallgatter, C., Shkurko, K., Rhodes, S., and Endries, J.: Orientations and aspect ratios of falling snow, *Geophys. Res. Lett.*, 42, 4617–4622, doi: 10.1002/2015GL064040, 2015.
- Hayden, L., and Liu, C. T.: A multiyear analysis of global precipitation combining CloudSat and GPM precipitation
535 retrievals, *J. Hydrometeorol.*, 19, 1925–1944, doi: 10.1175/JHM-D-18-0053.1, 2018.



- Heymsfield, A. J., Schmitt, C., Bansemer, A., and Twohy, C. H.: Improved representation of ice particle masses based on observations in natural clouds, *J. Atmos. Sci.*, 67, 3303-3318, doi: 10.1175/2010JAS3507.1, 2010.
- Heymsfield, A., Szakáll, M., Jost, A., Giammanco, I., and Wright, R.: A comprehensive observational study of graupel and hail terminal velocity, mass flux, and kinetic energy, *J. Atmos. Sci.*, 75, 3861-3885, doi: 10.1175/JAS-D-18-0035.s1, 540 2018.
- Haynes, J. M., Marchand, R. T., Luo, Z., Bodas-Salcedo, A., and Stephens, G. L.: A multipurpose radar simulation package: quick beam, *Bull. Amer. Meteor. Soc.*, 88, 1723-1727, doi: 10.1175/BAMS-88-11-1723, 2007.
- Haynes, J. M., L'Ecuyer T. S., Stephens G. L., Miller S. D., Mitrescu C., Wood N. B., and Tanelli S.: Rainfall retrieval over the ocean with spaceborne W-band radar, *J. Geophys. Res.*, 114, D00A22, doi:10.1029/2008JD009973, 2009.
- 545 Heymsfield, A. J., Schmitt, C., and Bansemer, A.: Ice cloud particle size distributions and pressure-dependent terminal velocities from in situ observations at temperatures from 0° to -86°C, *J. Atmos. Sci.*, 70, 4123-4154, doi: 10.1175/JAS-D-12-0124.1, 2013.
- Horie, H., Takahashi, N., Ohno, Y., Sato, K., Hayasaka, T., Nakamura, K., and Im, E.: Simulation for spaceborne cloud profiling Doppler Radar: EarthCARE/CPR, *Proc. SPIE 8523, Remote Sensing of the Atmosphere, Clouds, and Precipitation IV*, 8 Nov 2012, Kyoto, Japan, doi: 10.1117/12.977253, 2012.
- 550 Huang, G.-J., Bringi, V. N., Newman, G. L., Moisseev, D., and Notaros, B. M.: Dual-wavelength technique development for snow rate estimation: a case study from GCPEX, *Atmos. Meas. Tech.*, 12, 1409-1427, doi: 10.5194/amt-12-1409-2019, 2019.
- Illingworth A. J., Barker H. W., Beljaars A., Ceccaldi M., Chepfer H., Clerbaux N., Cole J., Delanoë J., Domenech C., Donovan D. P., Fukuda S., Hiraoka M., Hogan R. J., Huenerbein A., Kollias P., Kubota T., Nakajima T., Nakajima T. Y., Nishizawa T., Ohno Y., Okamoto H., Oki R., Sato K., Satoh M., Shephard M. W., Velázquez-Blázquez A., Wandinger, U., Wehr T and Van Z. G.: The EarthCARE Satellite: The Next Step Forward in Global Measurements of Clouds, Aerosols, Precipitation, and Radiation, *Bull. Amer. Meteor. Soc.*, 96, 1311-1332, doi: 10.1175/BAMS-D-12-00227.1, 2015.
- 555 Jung, Y., Zhang, G., and Xue, M.: Assimilation of simulated polarimetric radar data for a convective storm using the ensemble Kalman filter. Part I: observation operators for reflectivity and polarimetric variables, *Mon. Wea. Rev.*, 136, 2228-2245, doi: 10.1175/2007mwr2083.1, 2008.
- 560 Khain, A., and Pinsky, M.: *Physical processes in clouds and cloud modeling*. UK: Cambridge University Press, 2018.
- Kneifel, S., Maahn, M., Peters, G., and Simmer, C.: Observations of snowfall with a low-power FM-CW K-band radar (Micro Rain Radar), *Meteorol. Atmos. Phys.*, 113, 75-87, doi: 10.1107/s00703-011-0142-z, 2011.
- 565 Kollias, P., Clothiaux, E. E., Miller, M. A.: Millimeter-wavelength radars: new frontier in atmospheric cloud and precipitation research, *Bull. Amer. Meteor. Soc.*, 88, 1608-1624, doi: 10.1175/BAMS-88-10-1608, 2007.
- Lamer, K., Oue, M., Battaglia, A., Roy, R. J., Cooper, K. B., Dhillon, R., and Kollias, P.: Multifrequency radar observations of clouds and precipitation including the G-band, *Atmos. Meas. Tech.*, 14, 3615-3629, doi: 10.5194/amt-14-3615-2021, 2021.



- 570 Leinonen, J., Lebsock, M. D., Tanelli, S., Suzuki, K., Yashiro, H., and Miyamoto, Y.: Performance assessment of a triple-frequency spaceborne cloud-precipitation radar concept using a global cloud-resolving model, *Atmos. Meas. Tech.*, 8, 3493-3517, doi: 10.5194/amt-8-3493-2015, 2015.
- Li, R., Min, Q. L., Wu, X. Q., and Fu, Y. F.: Retrieving latent heating vertical structure from cloud and precipitation profiles-part II: deep convective and stratiform rain processes, *J. Quant. Spectrosc. Ra.*, 122, 47-63, doi: 10.1016/j.jqsrt.2012.11.029, 2013.
- 575 Lin, Y. L., and Colle, B. A.: A new bulk microphysical scheme that includes riming intensity and temperature-dependent ice characteristics, *Mon. Wea. Rev.*, 139, 1013-1035, doi: 10.1175/2010MWR3293.1, 2011.
- Liu, G. S.: A database of microwave single-scattering properties for nonspherical ice particles, *Bull. Amer. Meteor. Soc.*, 1563-1570, doi: 10.1175/2008BAMS2486.1, 2008.
- 580 Luo, Z. Z., Liu, G. Y., and Stephens, G. L.: CloudSat adding new insight into tropical penetrating convection, *Geophys. Res. Lett.*, 35, L19819, doi: 10.1029/2008GL035330, 2008.
- Mace, G., and Benson, S.: Diagnosing cloud microphysical process information from remote sensing measurements-A feasibility study using aircraft data. Part I: Tropical anvils measured during TC4, *J. Appl. Meteorol. Climatol.*, 56, 633-649. doi: 10.1175/JAMC-D-16-0083.1, 2017.
- 585 Marra, A. C., Marra, G. P., and Prodi, F.: Numerical scattering simulations for interpreting simultaneous observations of clouds by a W-band spaceborne and a C-band ground radar, *Eur. J. Remote Sens.*, 46, 909-927, doi: 10.5721/EuJRS20134654, 2013.
- Mason, B. J.: *The physics of clouds*, London: Oxford University Press, 1971.
- Mason, S. L., Chiu, C. J., Hogan, R. J., Moisseev, D., and Kneifel, S.: Retrievals of riming and snow density from vertically pointing Doppler radars, *J. Geophys. Res.*, 123, 807-834, doi: 10.1029/2018JD028603, 2018.
- 590 Mason, S. L., Hogan, R. J., Westbrook, C. D., Kneifel, S., Moisseev, D., and Terzi, L.: The importance of particle size distribution and internal structure for triple-frequency radar retrievals of the morphology of snow, *Atmos. Meas. Tech.*, 12, 4993-5018, doi: 10.5194/amt-12-4993-2019, 2019.
- Masunaga, H., Matsui, T., Tao, W.-K., Hou, A. Y., Kummerow, C. D., Nakajima, T., Bauer, P., Olson, W. S., Sekiguchi, M., and Nakajima, T. Y.: Satellite data simulator unit: a multisensor, multispectral satellite simulator package, *Bull. Amer. Meteor. Soc.*, 91, 1625-1632, doi: 10.1175/2010BAMS2809.1, 2010.
- 595 Matrosov, S. Y.: Modeling backscatter properties of snowfall at millimeter wavelengths, *J. Atmos. Sci.*, 64, 1727-1736, doi: 10.1175/JAS3904.1, 2007.
- Matsui, T., Iguchi, T., Li, X. W., Han, M., Tao, W. K., Petersen, W., L'Ecuyer, T., Meneghini, R., Olson, W., Kummerow, C. D., Hou, A. Y., Schwaller, M. R., Stocker, E. F., and Kwiatkowski, J.: GPM satellite simulator over ground validation sites, *Bull. Amer. Meteor. Soc.*, 94, 1653-1660, doi:10.1175/BAMS-D-12-00160, 2013.
- 600 Melnikov, V., and Straka, J.: Axis ratios and flutter angles of cloud ice particles: Retrievals from radar data, *J. Atmos. Ocean. Tech.*, 30, 1691-1703, doi: 10.1175/JTECH-D-12-00212.1, 2013.



- Miles, N. L., Verlinde, J., and Clothiaux, E. E.: Cloud droplet size distributions in low-level stratiform clouds, *J. Atmos. Sci.*, 57, 295-311, doi:10.1175/1520-0469(2000)057<0295:CDSDIL>2.0.CO;2, 2000.
- 605 Niu, S. J., and He, Z. Z.: Study on the water drop size distribution (WSD) in precipitous stratiform clouds, *Plateau Meteor.*, 14, 114-120, doi: CNKI:SUN:GYQX.0.1995-01-014, 1995.
- Nowell, H., Liu, G.S., Honeyage, R.: Modeling the microwave single-scattering properties of aggregate snowflakes, *J. Geophys. Res.*, 118, 7873-7885, doi: 10.1002/jgrd.50620, 2013.
- 610 Ray, P.: Broadband complex refractive indices of ice and water. *Appl. Opt.*, 11, 1836-1844, doi: 10.1364/AO.11.001836, 1972.
- Ryu, J., Song, H. -J., Sohn, B. -J., and Liu, C.: Global distribution of three types of drop size distribution representing heavy rainfall from GPM/DPR measurements, *Geophys. Res. Lett.*, 48, e2020GL090871, doi: 10.1029/2020GL090871, 2021.
- Ryzhkov, A., Pinsky, M., Pokrovsky, A., and Khain, A.: Polarimetric radar observation operator for a cloud model with spectral microphysics. *J. Appl. Meteorol. Climatol.*, 50, 873–894, doi: 10.1175/2010JAMC2363.1, 2011.
- 615 Ryzhkov, A. V., and Zrnich, D. S.: Radar polarimetry for weather observations, Cham, Switzerland: Springer Press, 2019.
- Sassen, K., Matrosov, S., and Campbell, J.: CloudSat spaceborne 94 GHz radar bright bands in the melting layer: an attenuation-driven upside-down lidar analog. *Geophys. Res. Lett.*, 34, L16818, doi: 10.1029/2007GL030291, 2007.
- Seto, S., Iguchi, T., Meneghini, R., Awaka, J., Kubota, T., Masaki, T., and Takahashi, N.: The precipitation rate retrieval algorithms for the GPM dual-frequency precipitation radar, *J. Meteor. Soc. Japan*, 99, 205-237, doi: 10.2151/jmsj.2020-010, 2021.
- 620 Stephens, G. L., Vane, D. G., Boain, R. J., Mace, G. G., Sassen, K., Wang, Z., Illingworth, A. J., O'Connor, E. J., Rossow, W. B., Durden, S. L.: The CloudSat mission and the A-train: a new dimension of space-based observations of clouds and precipitation, *Bull. Amer. Meteor. Soc.*, 83, 1771-1790, doi: 10.1175/BAMS-83-12-1771, 2002.
- 625 Stephens, G. L., Vane, D. G., Tanelli, S., Im, E., Suzuki, K.: CloudSat mission: Performance and early science after the first year of operation, *J. Geophys. Res.*, 113, D00A18, doi: 10.1029/2008JD009982, 2008.
- Stephens, G., Winker, D., Pelon, J., Trepte, C., Vane, D., Yuhas, C., L'Ecuyer, T. and Lebsock, M.: CloudSat and CALIPSO within the A-Train: Ten years of actively observing the Earth system, *Bull. Amer. Meteor. Soc.*, 99, 569-581, doi: 10.1175/BAMS-D-16-0324.1, 2018.
- 630 Sun, Y. T., Dong, X. Q., Cui, W. J., Zhou, Z. M., Fu, Z. K., Zhou, L. L., Deng, Y., and Cui, C. G.: Vertical structures of typical Meiyu precipitation events retrieved from GPM-DPR, *J. Geophys. Res.*, 125, e2019JD031466, doi: 10.1029/2019JD031466, 2020.
- Sy, O.O., Tanelli, S., Durden, S. L., Heymsfield, A., Bansemmer, A., Kuo, K.-S., Niamsuwan, N., Beauchamp, R.M., Chandrasekar, V., Vega, M., and Johnson, M.P.: Impact of mass-size parameterizations of frozen hydrometeors on microphysical retrievals: evaluation by matching radar to in situ observations from GCPEX and OLYMPEX, *J. Atmos. Oceanic Technol.*, 37, 93-112, doi: 10.1175/JTECH-D-19-0104.1, 2020.
- 635



- Szyrmer, W., and Zawadzki, I.: Snow studies. Part II: Average relationship between mass of snowflakes and their terminal fall velocity, *J. Atmos. Sci.*, 67, 3319–3335, doi: 10.1175/2010JAS3390.1, 2010.
- 640 Tanelli, S., Durden, S. L., Im, E.: CloudSat’s cloud profiling radar after two years in orbit: performance, calibration, and processing, *IEEE T. Geosci. Remote S.*, 46, 3560-3573, doi: 10.1109/TGRS.2008.2002030, 2008.
- Tanelli, S., Haddad, Z. S., Im, E., and Durden, S. L.: Radar concepts for the next generation of spaceborne observations of cloud and precipitation processes, *IEEE Radar Conference*, Oklahoma City, OK, USA, 23-27 April 2018, doi: 10.1109/RADAR.2018.8378741, 2018.
- 645 Tiira, J., Moisseev, D., Lerber, A., Ori, D., Tokay, A., Bliven, L., Petersen, W.: Ensemble mean density and its connection to other microphysical properties of falling snow as observed in southern Finland, *Atmos. Meas. Tech.*, 9, 4825–4841, doi: 10.5194/amt-9-4825-2016, 2016.
- Tinel, C., Testud, J., Pelon, J., Hogan, R. J., Protat, A., Delanoë, J., and Bouniol, D.: The retrieval of ice-cloud properties from cloud radar and lidar synergy, *J. Appl. Meteorol.*, 44, 860-875, doi: 10.1175/JAM2229.1, 2005.
- 650 Tomita, H.: New microphysical schemes with five and six categories by diagnostic generation of cloud ice, *J. Meteorol. Soc. Jpn.*, 86A, 121–142, doi:10.2151/jmsj.86A.121, 2008.
- Von Lerber, A., Moisseev, D., Bliven, L. F., Petersen, W., Harri, A.-M., and Chandrasekar, V.: Microphysical properties of snow and their link to Ze-S relations during BAecc 2014, *J. Appl. Meteorol. Climatol.*, 56, 1561–1582. doi: 10.1175/JAMC-D-16-0379.1, 2017.
- 655 Wang, Y., Han, T., Guo, J. C., Jiang, K., Li, R., Shao, W. C., Liu, G. S.: Simulation of the capability of Ku, Ka and W tri-frequency satellite-borne radar measuring the three-dimensional structure of cloud and precipitation, *Chin. Sci. Bull.*, 64, 430-443, doi: 10.1360/N972018-00089, 2019.
- Wood, N. B., L’Ecuyer, T. S., Heymsfield, A. J., and Stephens, G. L.: Microphysical constraints on millimeter-wavelength scattering properties of snow particles, *J. Appl. Meteorol. Climatol.*, 54, 909-931, doi: 10.1175/JAMC-D-14-0137.1, 2015.
- 660 Wu, Q., Yang, M. L., Dou, F. L., Guo, Y., An, D. W.: A study of cloud parameters retrieval algorithm for spaceborne millimeter wavelength cloud radar, *Acta Meteorol. Sin.*, 76, 160-168, doi: 10.11676/qxxb2017.07, 2018.
- Wu, Q., Hu, Y., Lu, N. M.: A simulation research on the wave bands selection of a satellite-borne rain measuring radar, *Acta Meteorol. Sin.*, 69, 344-351, doi: 10.11676/qxxb2011.029, 2013.
- 665 Yang, Z. L., Zhao, K., Xu, K., Li, K., Chen, G., Wen, L., Liu, S., and Yang, Z. W.: Microphysical characteristics of extreme convective precipitation over the Yangtze-Huaihe river basin during the Meiyu season based on polarimetric radar data, *Acta Meteorol. Sin.*, 77, 58-72, doi: 10.11676/qxxb2018.040, 2019.
- Yin, J. F., Wang, D. H., and Zhai, G. Q.: Long-term in situ measurements of the cloud-precipitation microphysical properties over East Asia, *Atmos. Res.*, 102, 206-217, doi: 10.1016/j.atmosres.2011.07.002, 2011.
- Zhang, G. F.: *Weather radar polarimetry*, New York, NY: CRC Press, 2017.



670

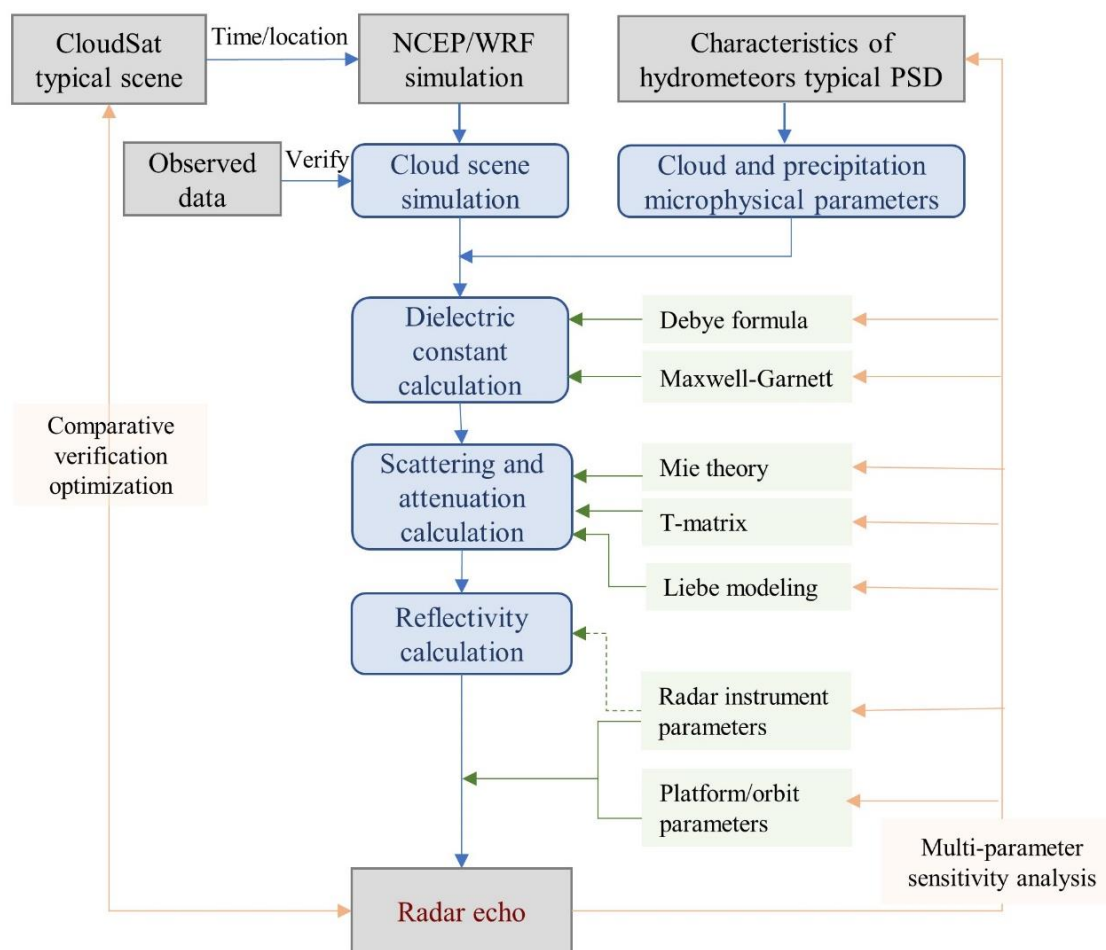
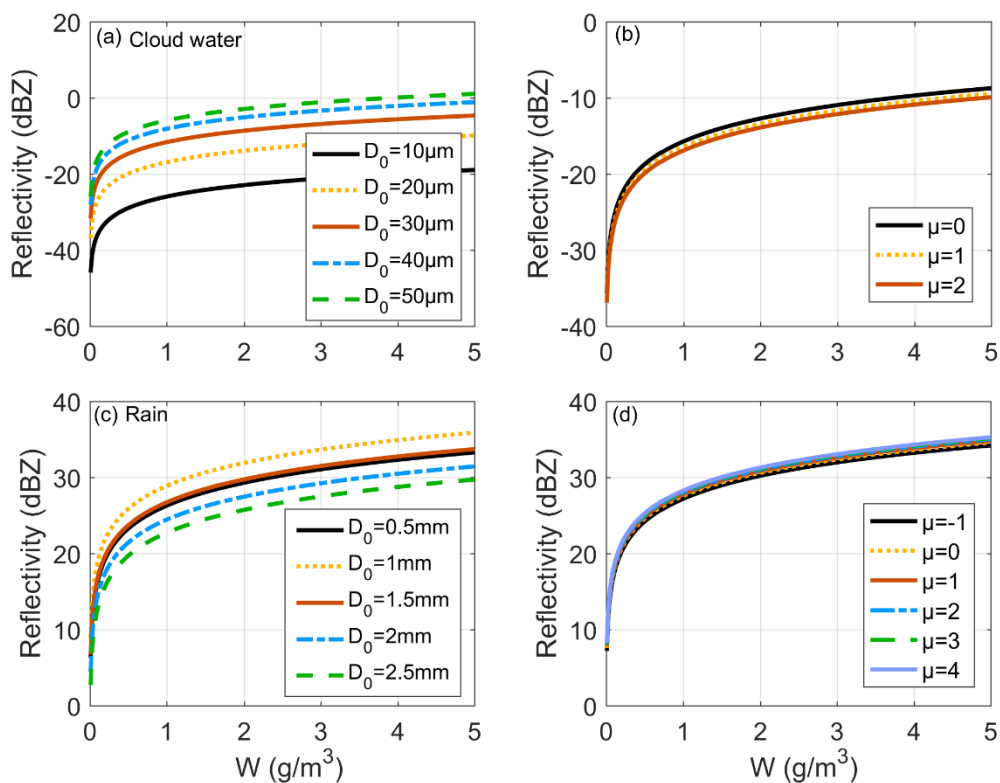
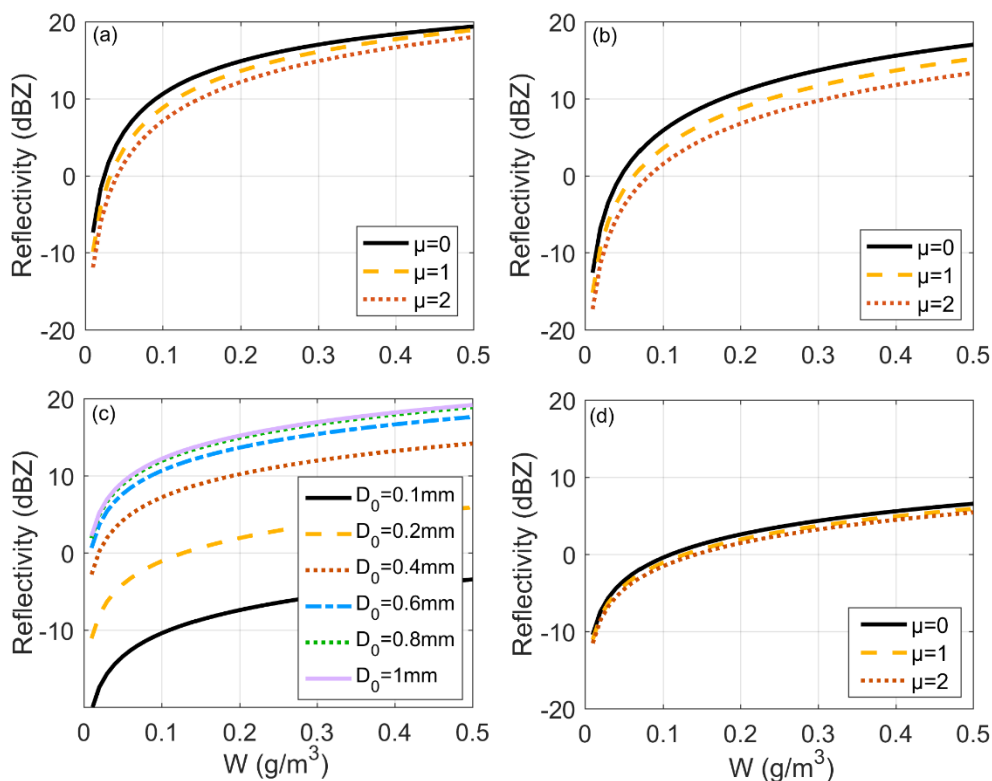


Figure 1: Sub module structure and logic framework of the simulation model

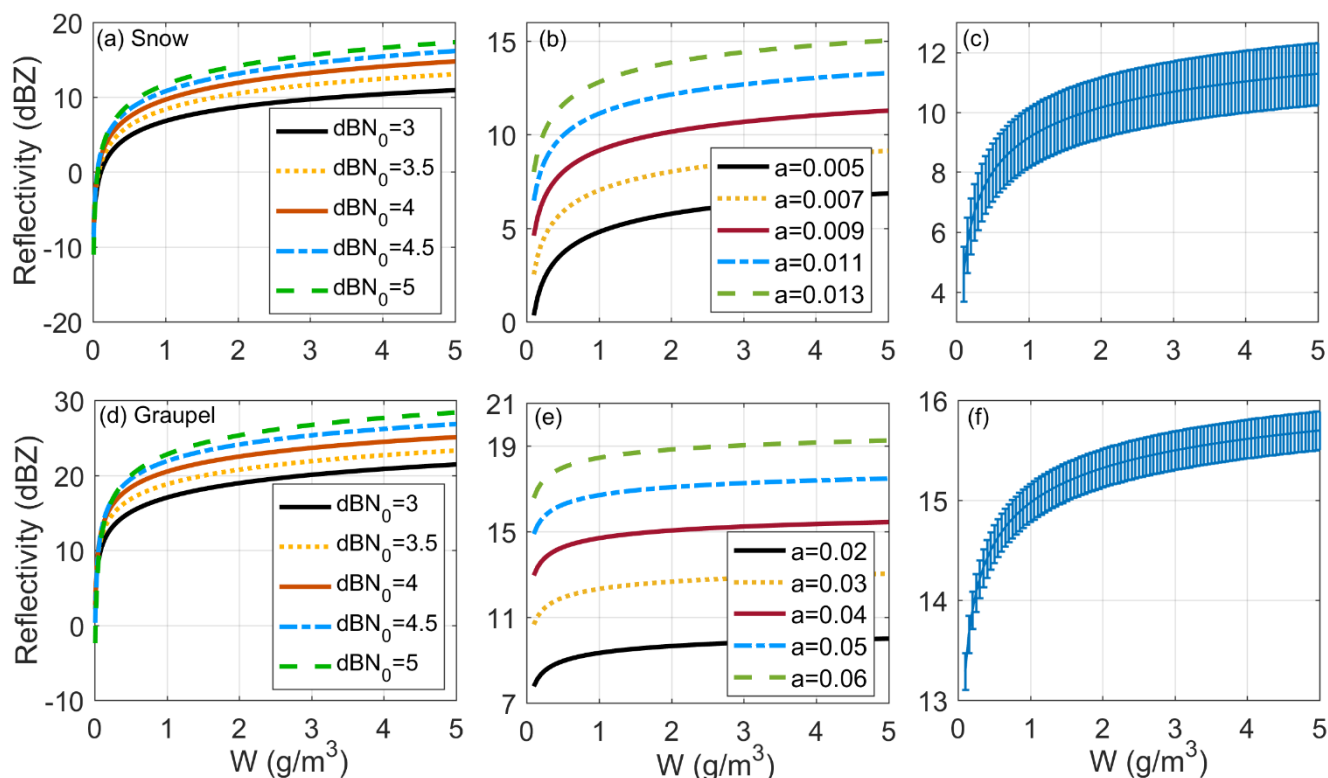


675 **Figure 2: Impact of the PSD parameters, i.e., D_0 and μ , on radar reflectivity for cloud water and rain. Reflectivity variation in cloud water caused by (a) D_0 of 10, 20, 30, 40, and 50 μm with a μ of 1 and (b) μ values of 0, 1, and 2 with D_0 of 20 μm . Reflectivity variation in rain caused by (c) D_0 of 0.5, 1, 1.5, 2, and 2.5 mm with a μ of 3 and (d) μ values of -1, 0, 1, 2, 3, and 4 with D_0 of 1.25 mm.**



680 **Figure 3: Impact of PSD parameters on radar reflectivity for cloud ice. PSD parameters constrained by Eqs. (7)–(9); reflectivity**
variation obtained when μ was 0, 1, and 2 and (a) temperature T was -20 °C and (b) T of -60 °C. PSD parameters varied
independently; reflectivity variation obtained by (c) D_0 of 0.1, 0.2, 0.4, 0.6, 0.8, and 1 mm with μ of 1 and (d) μ values of 0, 1, and
2 with D_0 of 0.2 mm.

685



690 **Figure 4: Impact of PSD parameters on radar reflectivity for snow and graupel. Variation in reflectivity for snow at (a) $\text{dB}N_0$ values of 3, 3.5, 4, 4.5, and 5 with a mean mass-diameter relationship of $m = 0.009D^{2.1}$, where D is in cm and m is in g; (b) prefactor a in mass-diameter relationship of 0.005, 0.007, 0.009, 0.011, and 0.013 g/cm^b , with exponent b of 2.1 and N_0 assumed to be $3 \times 10^3 \text{ m}^{-3} \text{ mm}^{-1}$; (c) mean value \pm standard deviation of b , where the mean is 2.1 and standard deviation (SD) is 0.5, with a assumed to be 0.009. The vertical bars denote the SD of the reflectivity change caused by deviation from the mean value of b . Variation in reflectivity for graupel at (d) $\text{dB}N_0$ values of 3, 3.5, 4, 4.5, and 5 with a mean mass-diameter relationship of $m = 0.04D^{2.6}$, where D is in cm and m is in g; (e) prefactor a in mass-diameter relationship of 0.02, 0.03, 0.04, 0.05, and 0.06 g/cm^b , with exponent b of 2.6 and N_0 assumed to be $4 \times 10^3 \text{ m}^{-3} \text{ mm}^{-1}$; and (f) mean value \pm standard deviation of b , where the mean is 2.6 and standard deviation is 0.3, with a assumed to be 0.04.**

695

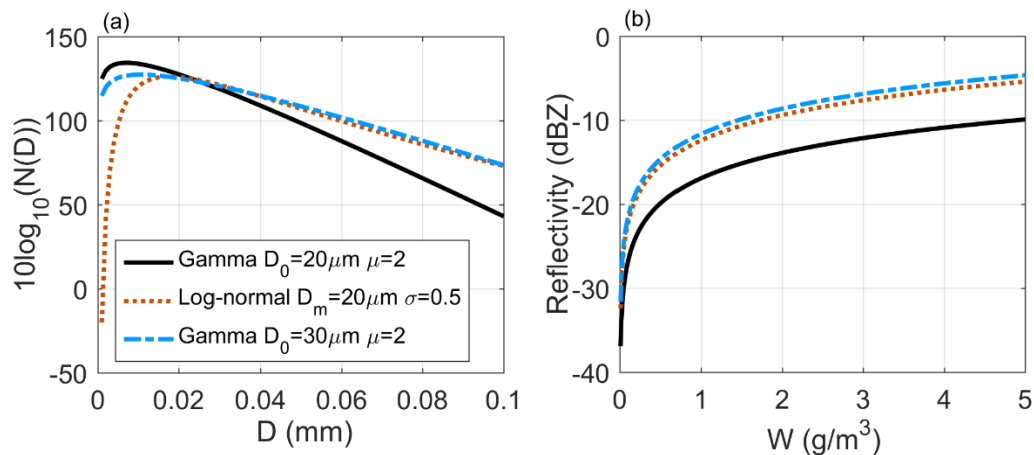


Figure 5: Impact of PSD models on radar reflectivity for cloud water. (a) Black solid line is for the gamma distribution: $W = 1$ (g/m^3), $D_0 = 20 \mu\text{m}$, and $\mu = 2$. Red-dotted line is for the log-normal distribution: $W = 1 \text{ g}/\text{m}^3$, $D_m = 20 \mu\text{m}$, and $\sigma = 0.5$. Blue-dashed line is for the gamma distribution: $W = 1 \text{ g}/\text{m}^3$, $D_0 = 30 \mu\text{m}$, and $\mu = 2$. (b) Variation in the radar reflectivity with W and the PSD models, where the PSD models are from (a).

700

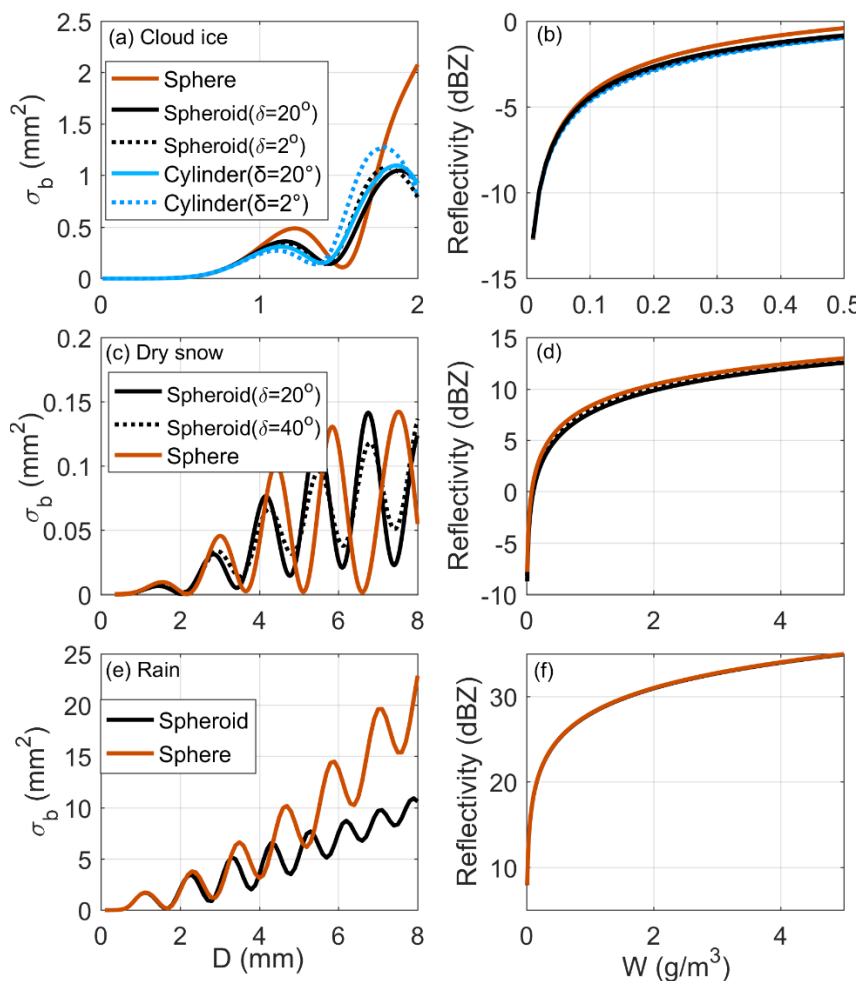
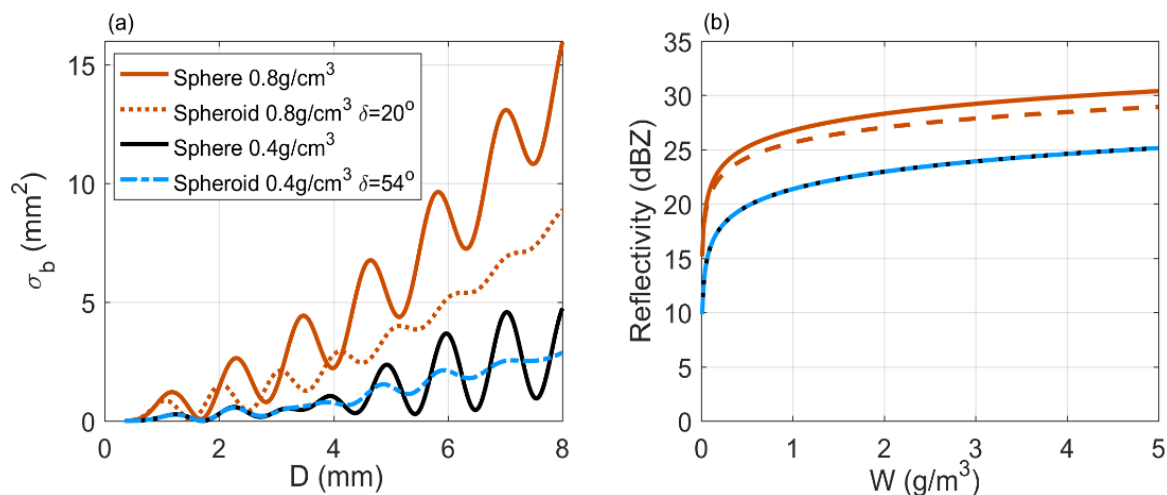


Figure 6: Backscattering cross-section and corresponding radar reflectivity under different shapes for cloud ice, dry snow, and rain. (a) Comparison of the backscattering cross-sections of ice crystals as spheres, spheroids, or cylinders, where δ is the SD of the canting angle. (b) Radar reflectivity comparison for particles in (a), where the PSD was assumed as a Gamma distribution constrained by Eqs. (7)–(9), with $\mu=1$ and $T = -60^\circ \text{ C}$. (c) Comparison of the backscattering cross-sections for dry snow with spheres and spheroids. (d) Radar reflectivity comparison for particles in (c), where the PSD was assumed as an exponential distribution with $N_0 = 3 \times 10^3 \text{ m}^{-3} \text{ mm}^{-1}$. (e) Comparison of backscattering cross-sections for raindrops with spheres and spheroids. (f) Radar reflectivity comparison for particles in (e), where the PSD was assumed as a Gamma distribution with $D_0 = 1.25 \text{ mm}$ and $\mu=3$.

705



710

Figure 7: Comparison of the backscattering cross-section and corresponding radar reflectivity for graupel between spheres and spheroids at different densities and orientations. (a) Backscattering cross-section at a density of 0.4 and 0.8 g/cm³ with δ (SD of canting angle) calculated from Eq. (14). After calculation, δ was 54° at a density of 0.4 g/cm³ while δ was 20° at a density of 0.8 g/cm³. (b) Radar reflectivity for particles in (a), where the PSD was assumed as an exponential distribution with N_0 of $4 \times 10^3 \text{ m}^{-3} \text{ mm}^{-1}$. Overestimation caused by the spherical assumption increased with an increase in density and decrease in δ .

715

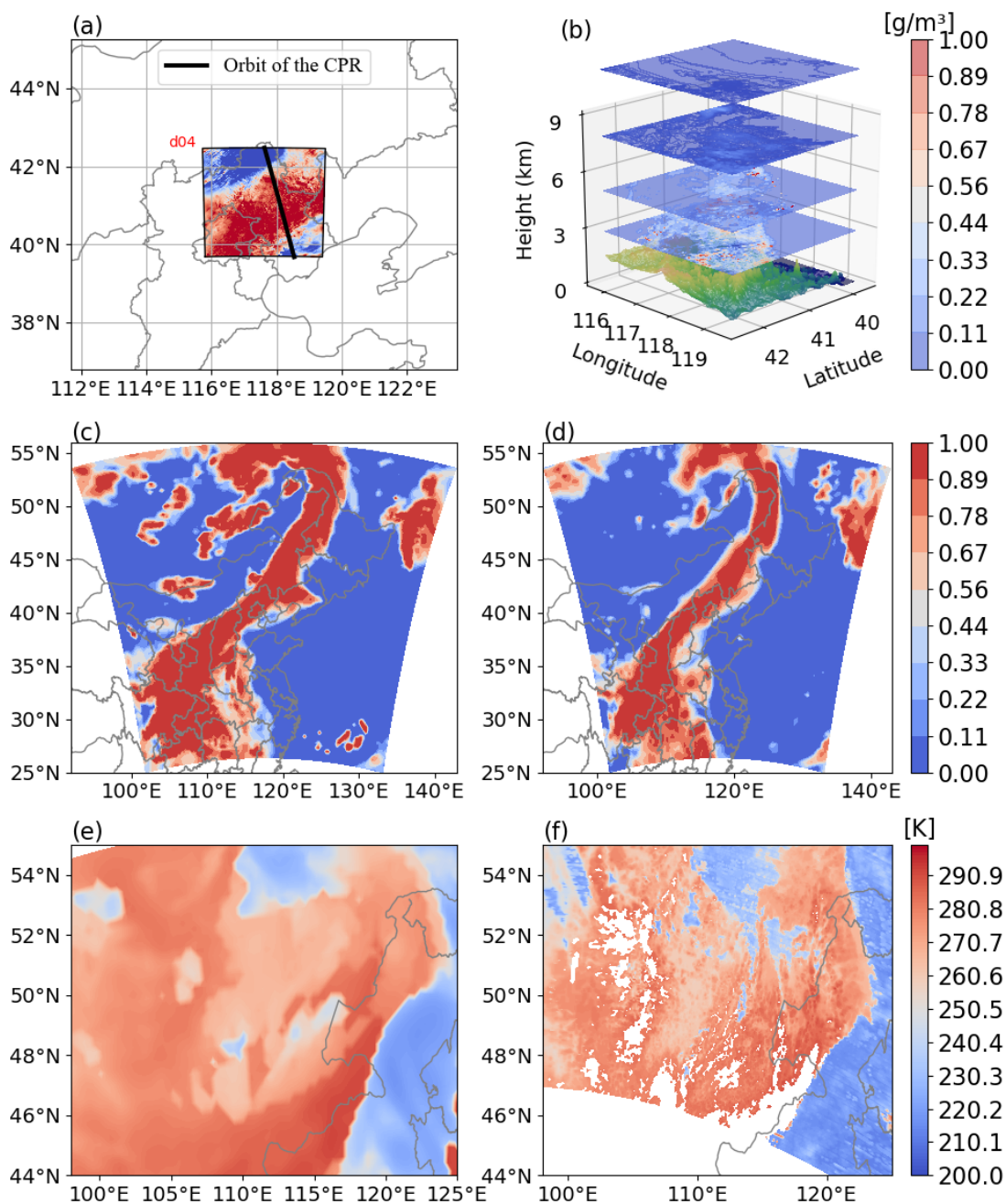


Figure 8: Simulation area exhibition of the stratiform cloud case scenario and comparison between the WRF simulation results and observation data. (a) Exhibition of the internal two-layer simulation area, (b) 3-D distribution of the total hydrometeor output from the WRF, (c) fraction of cloud cover from the WRF simulation, (d) fraction of cloud cover from the ERA5 data, (e) WRF model-simulated cloud top temperature, and (f) MODIS-observed cloud top temperature.

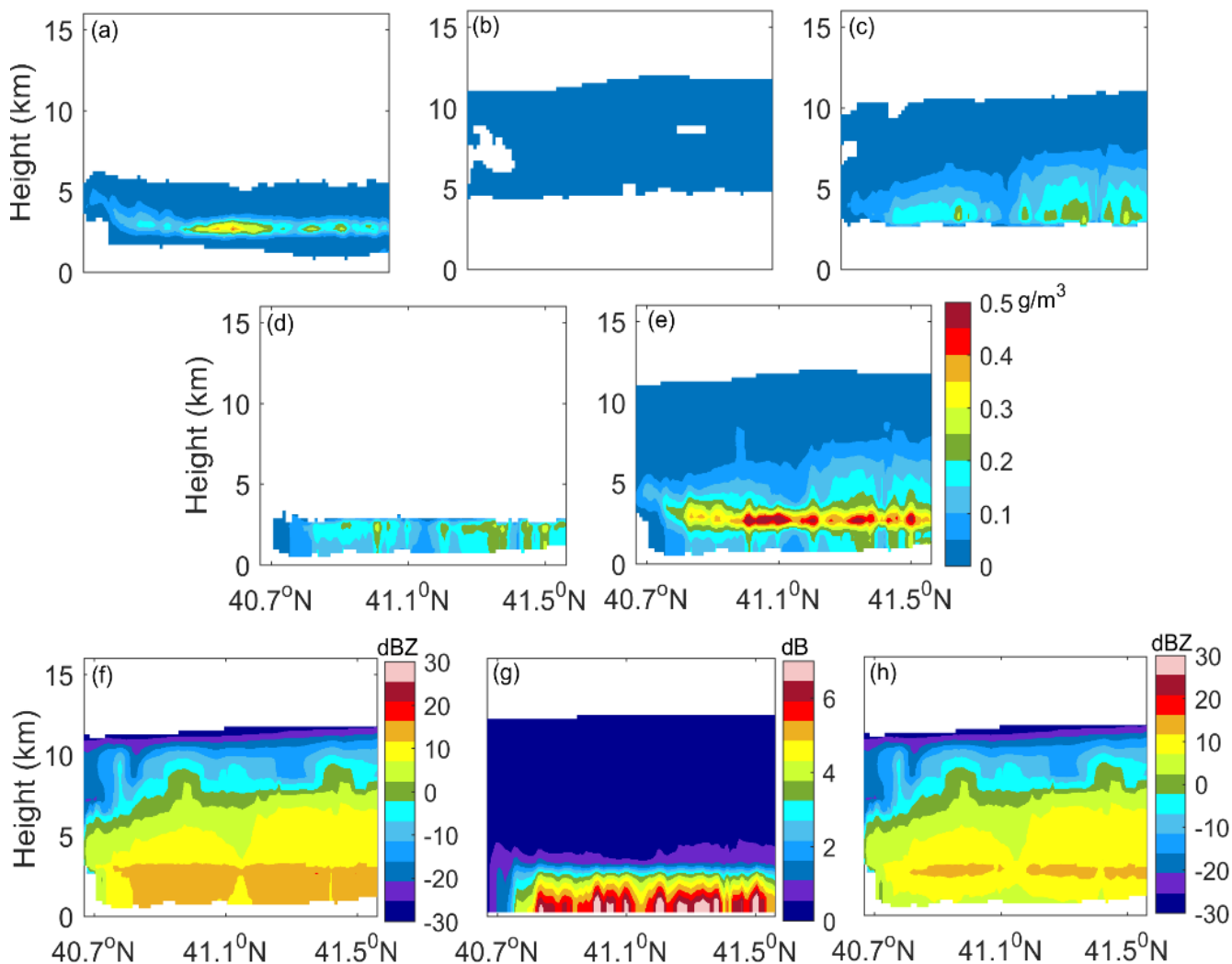
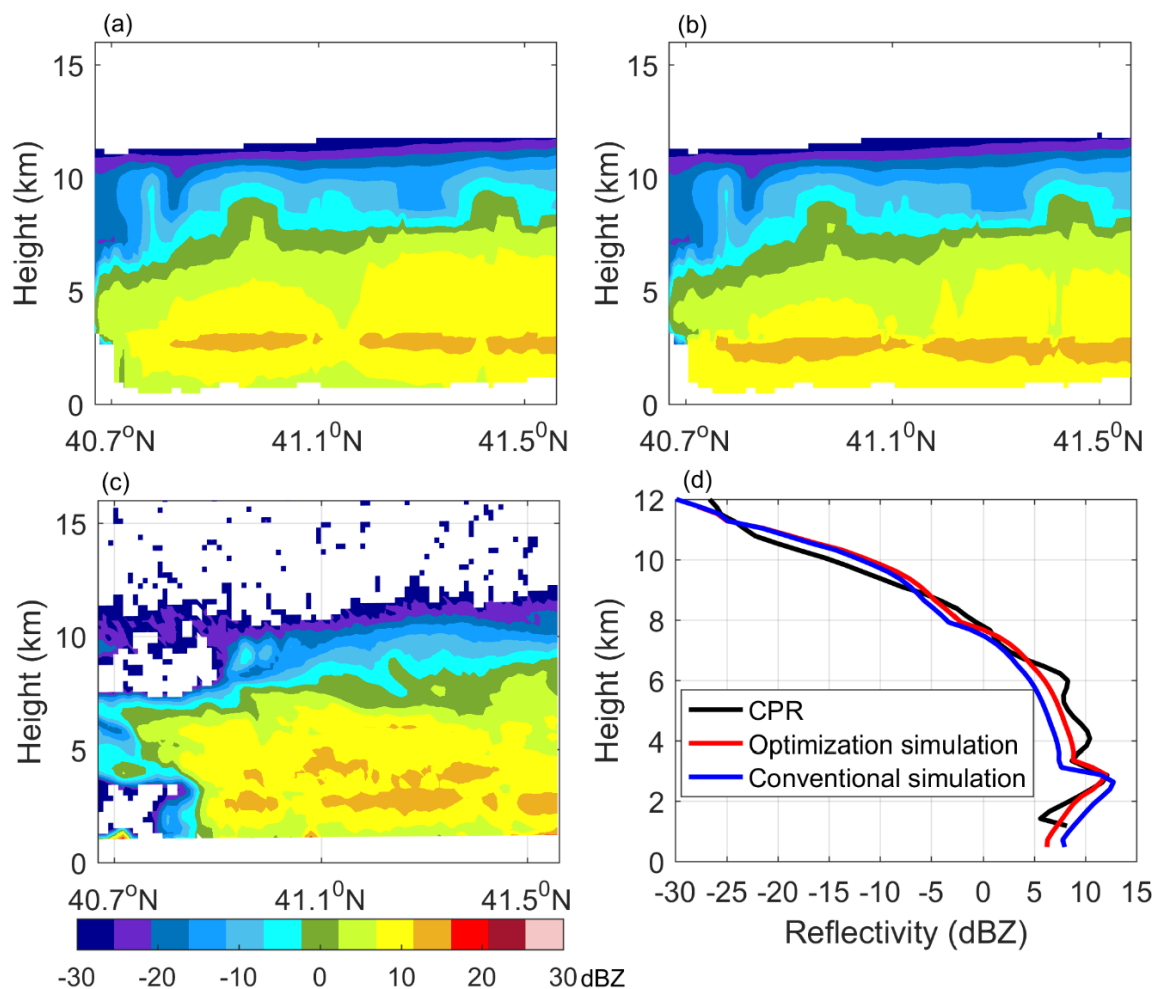
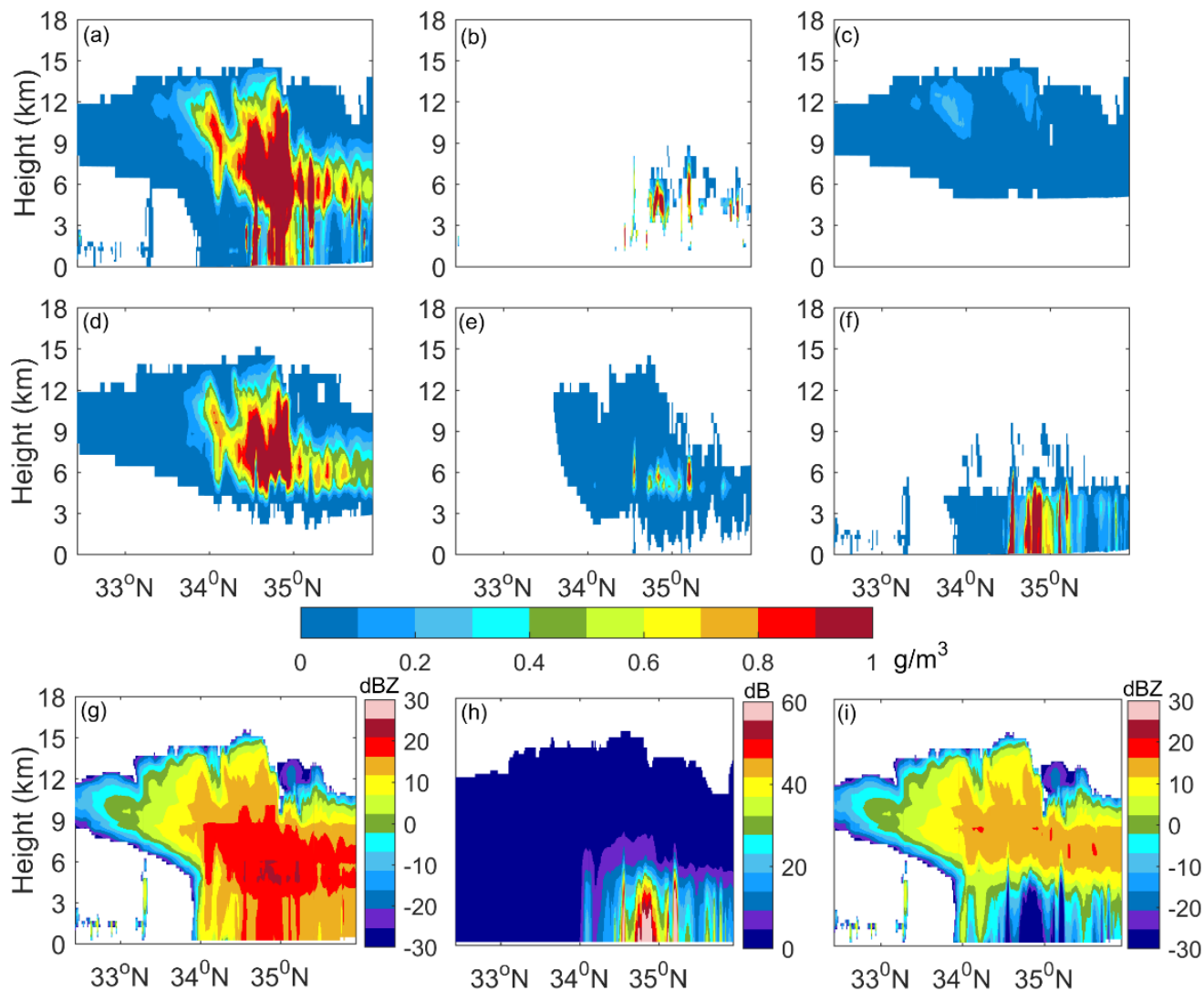


Figure 9: Latitude-height cross-section of the hydrometeor for the stratiform case simulated by the WRF for: (a) cloud water, (b) cloud ice, (c) snow, (d) rain, and (e) total hydrometeors. (f) Simulated radar reflectivity factor with the total hydrometeors before attenuation, (g) during attenuation, and (h) radar reflectivity factor after attenuation. Owing to the Mie scattering effect, the radar reflectivity did not decrease markedly at the bottom of the melting layer before attenuation, whereas the bright band at the melting layer was highlighted after attenuation due to strong attenuation in the rain region.

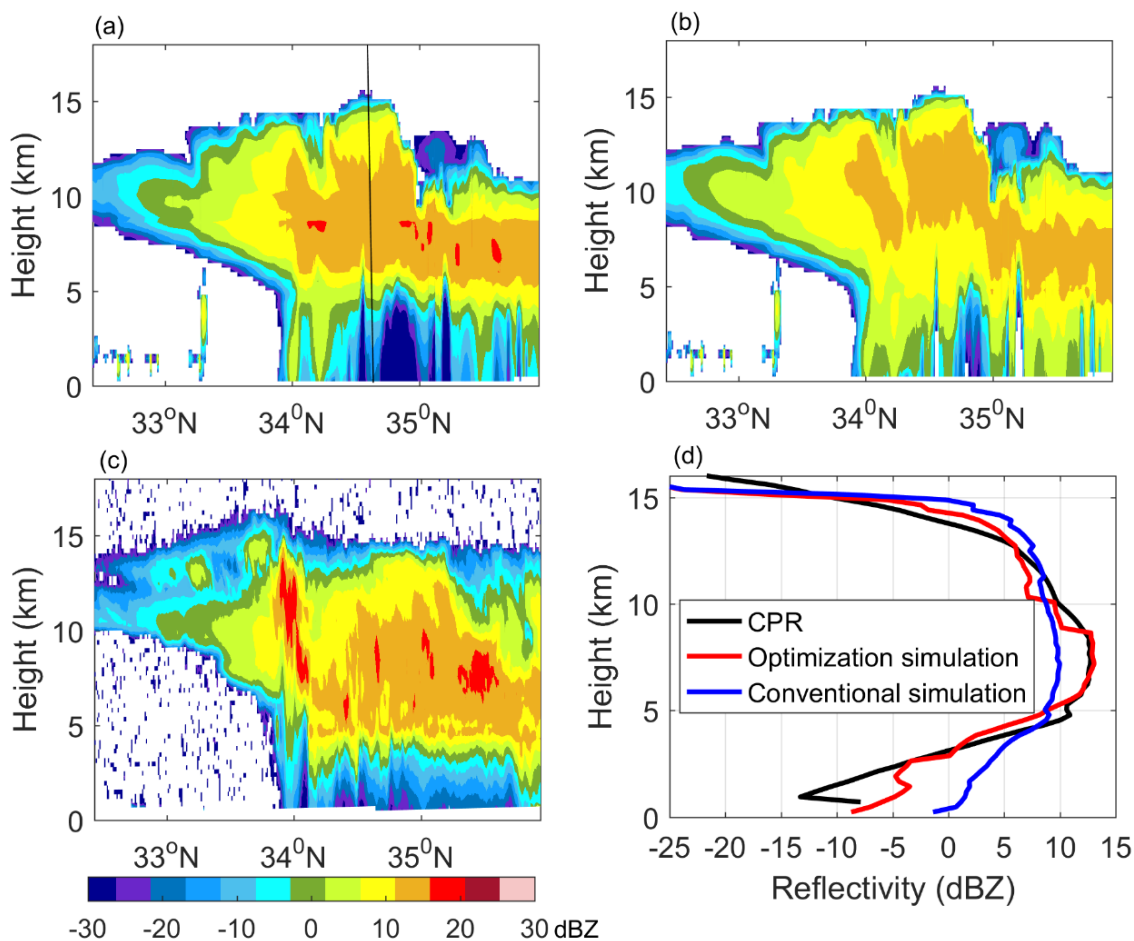
725



730 **Figure 10: Radar reflectivity comparison between the simulation results and CloudSat CPR observation data for the stratiform cloud precipitation case. (a) Cross-section of the simulation result with optimization settings, (b) cross-section of the simulation result with the conventional settings, and (c) cross-section of the CloudSat CPR observation data. (d) Vertical profiles of the average reflectivity in (a)–(c), where the red line denotes the simulation result with the optimization settings, the blue line denotes the simulation results with the conventional settings, and the black line denotes the results of the CPR observation. Owing to the melting modeling in the optimization simulation, the echo structure and intensity were consistent with the CPR observation results.**



735 **Figure 11: Latitude-height cross-section of the hydrometeor of the convective case simulated by the WRF for: (a) total hydrometeors, (b) cloud water, (c) cloud ice, (d) snow, (e) graupel, (f) rain. (g) Simulated radar reflectivity with the total hydrometeors before attenuation, (h) attenuation, and (i) radar reflectivity after attenuation**



740 **Figure 12: Radar reflectivity comparison between the simulation results and CloudSat CPR observation data for the convective case. (a) Cross-section of the simulation result with the optimization settings, (b) cross-section of the simulation result with the conventional settings using a fixed particle density, and (c) cross-section of the CloudSat CPR observation data. (d) Vertical profiles of the average reflectivity in (a)–(c), where the red line denotes the simulation result with the optimization settings, blue line denotes the simulation results with the conventional settings, and black line denotes the result of the CPR observation. The varying prefactor of density relations of snow and graupel due to the effect of riming was considered in the optimization simulation; the echo structure and intensity between the optimization simulation and CloudSat observation showed good agreement.**

745

750

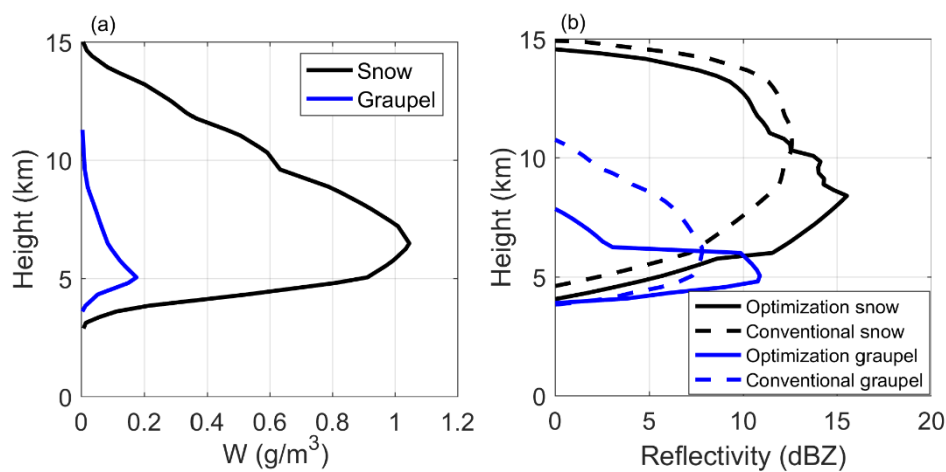


Figure 13: (a) Vertical profiles of water content for snow and graupel along black line in Fig. 12a, where black line denotes snow and blue line denotes graupel. (b) Corresponding reflectivity profiles with the optimization simulation and conventional simulation, where solid lines denote the simulation result with the optimization settings and dashed lines denote the simulation result with the conventional settings.

755